Inter-elemental osteohistological variation in *Massospondylus carinatus* and its implications for locomotion

Kimberley E J Chapelle Corresp., 1, 2 , **Paul M Barrett** 2, 3 , **Jonah N Choiniere** 2 , **Jennifer Botha** 4, 5

1 Division of Paleontology, American Museum of Natural History, New York City, New York, United States of America
2 Evolutionary Studies Institute, University of the Witwatersrand, Johannesburg, Gauteng, South Africa
3 Department of Earth Sciences, Natural History Museum, London, United Kingdom
4 Department of Zoology and Entomology, University of the Free State, Bloemfontein, Free State, South Africa
5 Karoo Palaeontology Department, National Museum, Bloemfontein, Free State, South Africa

Corresponding Author: Kimberley E J Chapelle
Email address: kimi.chapelle@gmail.com

Massospondylus carinatus Owen, 1854 is an iconic Early Jurassic basal sauropodomorph dinosaur from southern Africa that lived during the Early Jurassic. Over 200 specimens have been referred to the taxon, spanning the entire ontogenetic series from embryo to adult. Consequently, it provides an ideal sample for investigating dinosaur developmental biology, including growth patterns and growth rates, through osteohistological analysis. *Massospondylus carinatus* was the first early-branching sauropodomorph dinosaur for which a femoral growth series was sampled. Since then, growth series of other non-avian dinosaur taxa have shown that growth plasticity, intraskeletal variation, and ontogenetic locomotory shifts can complicate our understanding of growth curves and patterns. To investigate these questions further, it is necessary to sample multiple skeletal elements from multiple individuals across a large range of sizes, something that is hindered by incompleteness of the fossil record. Here, we conducted a broad, multi-element osteohistological study of long bones (excluding clavicles and metapodials) from 27 specimens of *Massospondylus carinatus* that span its ontogenetic series. Our study reveals substantial variations in growth history. A cyclical woven-parallel complex is the predominant bone tissue pattern during early and mid-ontogeny, which transitions to slower forming parallel-fibered bone during very late ontogeny. The bone tissue is interrupted by irregularly spaced cyclical growth marks (CGMs) including Lines of Arrested Growth (LAGs) indicating temporary cessations in growth. These CGMs show that the previously recorded femoral growth plasticity is also visible in other long bones, with a poor correlation between body size (measured by midshaft circumference) and CGM numbers. Furthermore, we found that the growth trajectory for an individual can vary depending on which limb element is studied. This makes the establishment of a definitive growth curve and determination of the onset of reproductive maturity difficult for this taxon. Finally, we found no evidence of differential growth rates in forelimb versus hind limb samples from the same individual, providing further evidence to falsify previously hypothesised ontogenetic postural shifts in *Massospondylus carinatus*.

Inter-elemental osteohistological variation in *Massospondylus carinatus* and its implications for locomotion

Kimberley E. J. Chapelle[1, 2]*, Paul M. Barrett[2,3], Jonah N. Choiniere[2], and Jennifer Botha[4,5]

[1]Division of Paleontology, American Museum of Natural History, Central Park West at 79th Street, New York, NY 10024-5192, USA

[2]Evolutionary Studies Institute, University of the Witwatersrand, 1 Jan Smuts Avenue, Johannesburg 2000, South Africa

[3]Department of Earth Sciences, Natural History Museum, Cromwell Road, London SW7 5BD, U.K.

[4]Karoo Palaeontology Department, National Museum, Bloemfontein, 9300, South Africa,

[5]University of the Free State, Department of Zoology and Entomology, Bloemfontein, 9300, South Africa

*Corresponding Author:
Kimberley E. J. Chapelle
Division of Paleontology, American Museum of Natural History, 200 Central Park West, New York, NY 10024, USA
Email address: kimi.chapelle@gmail.com

Abstract

Massospondylus carinatus Owen, 1854 is an iconic Early Jurassic basal sauropodomorph dinosaur from southern Africa that lived during the Early Jurassic. Over 200 specimens have been referred to the taxon, spanning the entire ontogenetic series from embryo to adult. Consequently, it provides an ideal sample for investigating dinosaur developmental biology, including growth patterns and growth rates, through osteohistological analysis. *Massospondylus carinatus* was the first early-branching sauropodomorph dinosaur for which a femoral growth series was sampled. Since then, growth series of other non-avian dinosaur taxa have shown that growth plasticity, intraskeletal variation, and ontogenetic locomotory shifts can complicate our understanding of growth curves and patterns. To investigate these questions further, it is necessary to sample multiple skeletal elements from multiple individuals across a large range of sizes, something that is hindered by incompleteness of the fossil record. Here, we conducted a broad, multi-element osteohistological study of long bones (excluding metapodials) from 27 specimens of *Massospondylus carinatus* that span its ontogenetic series. Our study reveals substantial variations in growth history. A cyclical woven-parallel complex is the predominant bone tissue pattern during early and mid-ontogeny, which transitions to slower forming parallel-fibered bone during very late ontogeny. The bone tissue is interrupted by irregularly spaced cyclical growth marks (CGMs) including Lines of Arrested Growth (LAGs) indicating temporary cessations in growth. These CGMs show that the previously recorded femoral growth plasticity is also visible in other long bones, with a poor correlation between body size (measured by midshaft circumference) and CGM numbers. Furthermore, we found that the growth trajectory for an individual can vary depending on which limb element is studied. This makes the establishment of a definitive growth curve and determination of the onset of reproductive maturity difficult for this taxon. Finally, we found no evidence of differential growth rates in forelimb versus hindlimb samples from the same individual, providing further evidence to falsify previously hypothesised ontogenetic postural shifts in *Massospondylus carinatus*.

Introduction

Massospondylus carinatus is the most abundant non-avian dinosaur known from southern Africa, and hundreds of specimens have been referred to it since its description in 1854 (Kitching, 1979; Kitching & Raath, 1984; Gow, Kitching & Raath, 1990; Sues *et al.*, 2004). *Massospondylus carinatus* has been found in the upper Elliot and Clarens formations of the Stormberg Group in South Africa and Lesotho as well as corresponding strata in Zimbabwe (i.e. Forest Sandstone and Mpandi formations) (Cooper, 1981; Kitching & Raath, 1984; Munyikwa, 1997; Catuneanu, Hancox & Rubidge, 1998; Bordy & Catuneanu, 2002; Rogers *et al.*, 2004; Barrett *et al.*, 2019). These stratigraphic layers are hypothesised to be Lower Jurassic in age (Blackburn *et al.*, 2013; Bordy & Eriksson, 2015; McPhee *et al.*, 2017; Bordy *et al.*, 2020). Phylogenetically, *Massospondylus carinatus* is part of the geographically widespread clade Massospondylidae (Chapelle & Choiniere, 2018). The large number of specimens, ranging in size from embryos to adults makes *Massospondylus carinatus* an ideal taxon for studying ontogenetic variation in dinosaurs (Gow, 1990; Chapelle & Choiniere, 2018; Neenan *et al.*, 2018; Chapelle *et al.*, 2019a; Chapelle *et al.*, 2019b; Chapelle, Fernandez & Choiniere, 2020; Chapelle, Botha & Choiniere, 2021). It has been hypothesised that *Massospondylus carinatus* underwent a locomotory shift, hatching as a quadruped and adopting bipedalism later in its development (Reisz *et al.*, 2005). However, recent studies on vestibular system morphology, and on forelimb to hindlimb ratios have found no evidence of this ontogenetic shift (Neenan *et al.*, 2018; Chapelle *et al.*, 2019b). Its position within the sauropodomorph phylogenetic lineage, combined with its abundance and stratigraphic age, make *Massospondylus carinatus* an important taxon for better understanding early dinosaur evolution and the palaeoecology of Early Jurassic ecosystems.

For nearly two centuries, osteohistology has been recognised as a useful tool for studying life history traits in dinosaurs, including growth rates (Erickson, Rogers & Yerby, 2001; Erickson, 2005; Lehman & Woodward, 2008), metabolic rates (Sander & Klein, 2005; Erickson *et al.*, 2009), and the onset of sexual maturity (Erickson *et al.*, 2007; Lee & Werning, 2008). Chinsamy's (1993) study on a size series of *Massospondylus carinatus* femora was the first detailed work on basal sauropodomorph osteohistology (Chinsamy, 1993; Klein & Sander, 2007). This study found that growth rate decreased with age, but that growth did not cease completely (Chinsamy, 1993; Klein & Sander, 2007). Chinsamy (1993) also concluded that the taxon displayed a cyclical (based on the presence of growth marks in the cortical bone) and indeterminate growth strategy (based on the absence of a true outer circumferential layer [= external fundamental system]), suggesting an intermediate physiology between ectothermy and endothermy (Chinsamy, 1993; Klein & Sander, 2007).

Since then, osteohistology has also been used to examine locomotory shifts in dinosaurs by relating forelimb to hindlimb ratios to age (such as a shift from quadrupedalism to bipedalism in *Psittacosaurus* (Zhao *et al.*, 2013)). Osteohistological studies of intraspecific ontogenetic series have been carried out across the dinosaur tree, using different postcranial elements including: size series of femora (Chinsamy, 1993; Klein & Sander, 2007; Skutschas *et al.*, 2021); strictly or mostly stylopodial elements (Sander, 1999; Klein & Sander, 2008); and mixed postcranial elements, including limb bones and ribs (Erickson *et al.*, 2006; Werning, 2012; Stein, Hayashi & Sander, 2013; Cerda, Pol & Chinsamy, 2014).

Recent work has highlighted some caveats in estimating dinosaur growth curves. Taxon misidentification, errors in age estimates and when retro-calculating missing Cyclical Growth Marks (CGMs) or Lines of Arrested Growth (LAGs), the lack of data points in an ontogenetic sample, as well as the scarcity of fully mature specimens warrant caution in model-based studies of dinosaur growth (Myhrvold, 2013). Growth strategies have also been found to be divergent in dinosaurs, with both acceleration and hypermorphosis models having been hypothesised in theropods, for example (Cullen *et al.*, 2020). Furthermore, the relationship between LAG spacing and organismal growth has been found to be inconsistent, with intra-elemental variation leading to markedly different conclusions regarding the relative maturity of specimens depending on which area of the bone was analysed (Cullen *et al.*, 2021). Further uncertainties arise when comparing different elements from a single individual due to intra-skeletal variation in LAG counts (Cullen *et al.*, 2021). Archosaurs have been found to show intraskeletal variation in growth rates, with the femora, tibiae and humeri growing faster than other limb elements. LAG counts also vary between elements (Curry, 1999; Woodward, Horner & Farlow, 2014). Finally, osteohistological growth plasticity (hereafter 'growth plasticity') further exacerbates the difficulty of estimating ages and determining growth patterns in dinosaurs.

A recent study on *Massospondylus carinatus* found high variability in LAG spacing that provided evidence for growth plasticity with disparate body masses for *Massospondylus carinatus* individuals at given ontogenetic ages (Chapelle, Botha & Choiniere, 2021). This suggested that traditional sigmoidal growth curves and inflection-based estimates of sexual maturation are not useful for this taxon. Similar growth plasticity has been recorded in *Plateosaurus trossingensis* and *Mussaurus patagonicus*, with histological features correlating poorly with body size and possibly being influenced by environmental factors instead (Sander & Klein, 2005; Klein & Sander, 2007; Cerda et al., 2022 in press). These confounding issues for interpreting osteohistology warrant caution and have led to a series of recommendations, including: increasing sample sizes for the individuals in a single ontogenetic series; incorporating tissue organization and vascularity changes into these analyses; and multi-element sampling (Cullen *et al.*, 2021).

A revised set of diagnostic criteria for *Massospondylus carinatus* (Chapelle & Choiniere, 2018; Barrett *et al.*, 2019), new specimens referrable to the genus, and recent stratigraphic revisions (Viglietti *et al.*, 2020) invite a reconsideration of *Massospondylus carinatus* growth. Here, we present the results of a broad, multi-element, multi-ontogenetic stage study that aims to: 1) answer questions about intraskeletal variation during ontogeny; 2) test previously proposed growth curves; and 3) to determine if a locomotory shift is recorded in the bone microstructure.

Methods

A destructive sampling permit (permit number 2643) was acquired from the South African Heritage Resources Agency (SAHRA) in order to sample long bones from 27 *Massospondylus carinatus* specimens. The sectioned sample is composed of 50 elements: 15 humeri, two radii, two ulnae, 19 femora, 10 tibiae, and two fibulae (see Table 1).

All osteohistological sections were produced at the National Museum, Bloemfontein following standard methods (Botha-Brink, Soares & Martinelli, 2018). Two-to-three-centimetre-thick blocks were cut out of the long bone midshafts using a handsaw and Dremel® tool. These blocks were embedded in Struers EpoFix® resin under vacuum and dried for at least 24 hours. They were then cut (using a Struers Accutom-100®) into 1.5 mm-thick cross-sections. Thick sections were stuck to 5 mm-thick glass and plastic slides with EpoFix® resin, and ground to a few microns in thickness using a Struers Accutom-100®. Rendering was carried out under normal (NL), polarised (PL) and cross-polarised (CPL) light, using polarizing microscopes (Nikon Eclipse Ci-POL) equipped with a digital camera (DS-Fi3), in NIS-Elements 4.5 (Nikon Corp., Tokyo, Japan). Stitched images of complete transverse sections were assembled using NIS-Elements. The smallest specimen in the study, the embryonic individual BP/1/5347a, was studied using digital osteohistological data (for the humerus, radius, ulna, femur, tibia and fibula) obtained using synchrotron radiation X-ray micro-computed tomographic (SRµCT) scanning done at the European Synchrotron Radiation Facility (Grenoble, France) with an isotropic voxel size of 13.11 µm.

Minimum circumferences were taken at the midshaft of each fore- and hindlimb bone using tailoring tape. For elements that were already embedded and sectioned, circumferences were measured using ImageJ 1.52a (Schneider, Rasband & Eliceiri, 2012). For seven individuals that only preserved a partial femur or which did not preserve a femur at all, a femoral circumference was estimated using the regression of LOG(minimum femoral circumference) to LOG(minimum humeral circumference), which are highly correlated in *Massospondylus carinatus* with a R^2 value of 0.9951 (see fig. S1). For two specimens that lacked a humerus, a femoral circumference was estimated using the regression of LOG(minimum femoral circumference) to LOG(minimum tibial circumference), which are highly correlated in *Massospondylus carinatus* with an R^2 value of 0.9907 (see fig. S2).

For ease of description, the sample was arbitrarily divided into four size classes (SC) based on relative femoral size percentage (i.e. minimum femoral shaft circumference) when compared to the largest specimen in the sample (BP/1/4934): 0–25% are considered to be SC1 individuals; 26–50% are SC2; 51–75% are SC3; and 76–100% are SC4 (see Table 1). The proportional size of the specimens relative to the skeletally mature BP/1/4934 (Barrett *et al.*, 2019) is referred to as % size for brevity. Traditionally % of the largest known specimen (or % size) is used to sort elements into ontogenetic stages *a priori*. However, given the extreme growth plasticity seen in *Massospondylus carinatus*, where size is decoupled from age, we were unable to divide the bones into discrete ontogenetic categories (Chapelle, Botha & Choiniere, 2021).

Five-to-ten times magnification (x10) images were taken in the mid-cortex of each bone. Vascular canals were then identified and their surface area measured in ImageJ 1.52a (Schneider, Rasband & Eliceiri, 2012). Proportional vascularisation was then calculated by dividing the canal surface area by the total surface area of the field of view. The mean vascularisation of these measurements was then calculated for each bone (Tables 2-3, Table S1).

An overlapping growth series of femora was selected to retro-calculate the number of LAGs missing due to resorption and remodelling (BP/1/5347, BP/1/5253, BP/1/4266, BP/1/5241 and BP/1/4934). Growth curves were generated for all specimens, as well as for the overlapping growth series, using LAG radius as a proxy for body mass. Incomplete cortical surfaces of several specimens including the largest specimen (BP/1/4934) in the sample precluded use of LAG circumference as a body mass proxy (Cullen *et al.*, 2021). Nevertheless, comparisons of the LAG radii in the thickest part of the cortex to their circumferences provides similar metrics for inferring growth (see fig. S3 and table S2). Due to the irregular spacing between LAGs and the lack of correlation between size and number of LAGs, a minimum and maximum age were calculated using the longest and shortest distances between LAGs (respectively) (see table S3).

Body mass (BM) estimates were made by applying the formula ($\log BM=2{,}754*\log_{10}$[femoral circumference]-0,683) developed by Campione *et al*. (2014) for inferring BM using minimum femoral circumferences for bipedal taxa.

All linear measurements using the histological sections were made using ImageJ 1.52a (Schneider, Rasband & Eliceiri, 2012) and the figures were generated in R Studio Version 1.1.453 (Team, 2016) and Inkscape (Harrington et al., 2004–2005).

Results

General description of bone microstructure

The following descriptions of the bone microstructure are organized by element and size class (figs 1–9). We include here a summarized table of morphologies, definitions and abbreviations for ease of reading the descriptive section (Table 4). The nomenclature presented in this table and used to describe bone matrices, bone tissue types and vascular arrangements was taken from the recently published textbook edited by de Buffrénil *et al*. (2021).

The SRµCT scans of the embryonic BP/1/5347a were sufficient and useful to look at medullary cavity and cortical thicknesses, as well as vascularisation. However, osteocytes could not be observed. The embryonic transverse sections all show large, open medullary cavities. The cortices are highly vascularised with large vascular channels, and although further details regarding the bone tissues cannot be observed, the cortex is likely formed from woven bone, as is found in all other neonate dinosaurs studied to date (Horner & Currie, 1994; Horner, De Ricqlès & Padian, 2000; Reisz *et al.*, 2013) (fig. S4).

Humeri

Two SC1 humeri were available for study (BP/1/5347a and BP/1/5253; minimum circumferences of 3.61 mm and 29.5 mm, respectively). The smaller of the two is an embryonic specimen. In the latter, the medullary cavity is open and there are no visible trabeculae. The tissue is azonal, with no identifiable LAGs or annuli. There is no distinct change between the inner and outer cortical tissue pattern (fig. 1A). The bone tissue is WFB with primary osteons indicating the presence of WPC (Stein & Prondvai, 2014; de Buffrénil *et al.*, 2021) (fig. 1E). The vascularisation is laminar in arrangement.

There are two SC2 humeri, BP/1/4266 and BP/1/4751, with minimum circumferences of 46 mm and 52 mm, respectively (fig. 1). The medullary cavity is open and very few trabeculae are visible. Both specimens have very large- to medium-sized resorption cavities in the inner cortex, which decrease in size and scatter into the mid-cortex (fig. 1C and 1D). The bone tissue in the inner cortex is FLC (this sub-category of WPC indicates very rapid growth) with a mixture of longitudinal, laminar and plexiform primary osteons (fig. 1D). The mid-cortex is WPC (fig. 1E). This region varies in vascular arrangement between humeri. BP/1/4266cA has a vascular arrangement that is mainly longitudinal with some short anastomoses in places. BP/1/4751 has a mixture of laminar, reticular and longitudinal vascular arrangements in the mid-cortex. In BP/1/4266, the orientation of the vascular canals in the outer cortex is longitudinal with some short anastomoses in places, unlike BP/1/4751A, which appears to be much less vascularised (fig. 1F). The bone tissue in the outer cortex of these specimens is still WPC. Bands of parallel-fibred bone are observed before and after the LAGs, indicating the presence of annuli in BP/1/4751A (fig. 1E, 1F, and 1G). Both specimens have zonal bone tissue with three (BP/4266) and five (BP/1/4751) LAGs observed (table 2). These LAGs are often irregularly spaced: they do not decrease in spacing towards the sub-periosteal surface in BP/1/4266 but do in BP/1/4751 (fig. 11).

There are eight SC3 humeri, which range from 72–101 mm in minimum circumference (with NMQR 3055 and BP/1/5005 representing the smallest and largest in the sample, respectively, table 1). The medullary cavity is open in all SC3 humeri and large-to-medium-sized resorption cavities line the perimedullary region with smaller resorption cavities scattered through the mid-cortex (except in BP/1/5241 where the resorption cavities are restricted to the inner cortex) (fig. 2A and 2B). BP/1/4998 lacks resorption cavities. The inner cortex matrix of the smaller specimens in SC3 is composed of a WPC. In these specimens, the vascularisation of the inner and outer cortex does not vary much and the vascular arrangement is laminar mixed with longitudinal canals. BP/1/4860A has a mainly plexiform vascular arrangement in the inner and mid-cortex although this might have been exaggerated by diagenesis (fig. 2A). Larger SC3 specimens contain WPC. They also have a laminar vascular arrangement mixed with longitudinal primary osteons. BP/1/4999 mainly has large primary osteons with some short circumferentially-oriented anastomoses in places. BP/1/5005 (the largest SC3 specimen) is highly remodelled with many secondary osteons, and it is thus difficult to determine vascular arrangements (fig. 2B). The mid-cortex of larger SC3 specimens appears slightly less vascularised than the inner cortex and mostly comprises longitudinally-oriented vascular canals with short oblique or circumferentially-oriented anastomoses. BP/1/5005 has a mid-cortex consisting of a WPC and alternating bands of slightly more vascularised reticular canals with slightly less vascularised bands of longitudinal primary osteons and short anastomoses in places (fig. 2C). These SC3 specimens contain WPC all the way to the outermost cortex (see BP/1/4998, figs. 2D and 2E). Smaller SC3 specimens have a highly vascularised outer cortex with a mix of laminar and longitudinally-arranged canals. Larger SC3 specimens appear to be slightly less vascularised in the outer cortex with a mix of laminar and longitudinal canals (BP/1/4998 has a patch of short oblique anastomoses connecting the longitudinal canals). Larger SC3 specimens are also much less vascularised and mainly have longitudinally-oriented primary osteons at the sub-periosteal surface (see BP/1/5241 and BP/1/5005, see figs. 2E and 2G). All SC3 specimens have zonal bone tissue with the presence of 3–14 LAGs (the larger specimens do not necessarily have the most LAGs; see table 2). These LAGs are often irregularly spaced (fig. 11) and do not decrease in spacing towards the sub-periosteal surface except in NMQR 3964 and BP/1/5193, which have regularly spaced LAGs that decrease in spacing towards the outer cortex. Several specimens have double and triple LAGs (BP/1/4860, BP/1/5241 and BP/1/5005; see figs. 2F and 2G). The LAGs are usually associated with annuli of parallel-fibred bone or lamellar bone (figs. 2E and 2G). Three of the specimens have Sharpey's fibres (representing muscle attachment as defined by Francillon-Vieillot et al., 1990), which are best seen in cross-polarised light (BP/1/4860, BP/1/4999 and BP/1/5241; see fig. 2H). These are very extensive in

BP/1/4860A although this section was taken closer to the deltopectoral crest than in the other humeri sampled.

There are four SC4 humeri in the sample ranging from 103–141 mm in circumference (BP/1/5397 and BP/1/4934A representing the smallest and largest, respectively). The medullary cavity is open with small broken trabeculae in the perimedullary region. Three of the specimens have small to large-sized resorption cavities in the perimedullary region and inner cortex (resorption cavities are absent in BP/1/5000) (fig. 3A and 3B). All three specimens have secondary osteons in the inner cortex (fig. 3A, 3B and 3C). These are sparsely distributed in BP/1/5397 or BP/1/6125 and densely distributed in the other two specimens (i.e. BP/1/5000 and BP/1/4934). The vascularisation and matrix of the inner cortex are difficult to ascertain due to the remodelling in the two larger specimens. The smaller BP/1/5397 and BP/1/6125 are less remodelled and show WPC throughout the cortex. They contain a mixture of longitudinally-oriented primary osteons and a laminar arrangement of canals in the inner cortex (fig. 3B and 3C). The mid-cortex of the SC4 specimens is also of the WPC type and mainly exhibits a mixture of laminar and plexiform vascularisation (fig. 3D). The outer cortex is much less densely vascularised with higher amounts of parallel-fibred bone within the WPC (fig. 3E). All of the specimens have zonal bone with 5–10 LAGs usually associated with LB or PFB (figs. 3E and 3F). These do not decrease in spacing except in BP/1/6125 (fig. 5D). However, an EFS was not observed in any SC4 specimen. Two of the specimens have double and triple LAGs (BP/1/6125 and BP/1/4934). BP/1/6125 and BP/1/4934 also have Sharpey's fibres.

Radii

There are only three radii in the sample. The smallest is that of the embryo BP/1/5347a (1.88 mm in circumference). The second is in SC2, BP/1/4376 (21.5 mm in circumference). The medullary cavity of this specimen is open. The entire cortex is comprised of a woven matrix (fig. 4A). The inner and mid-cortex show little variation in vascularisation with the vascular canals being mostly longitudinally-oriented primary osteons with some short oblique and transverse anastomoses in places, thus forming a WPC (fig. 4A). There is a thick band of bone in the mid-cortex, which has very little vascularisation. The outer cortex has mainly longitudinally-oriented primary osteons with short circumferential anastomoses in some areas. There are no visible LAGs in the section. Short Sharpey's fibres are visible throughout the section (fig. 4A).

The third radius, BP/1/5011, has a minimum circumference of 81 mm. This is similar in size to the radius of BP/1/4934, which was not sampled in this study (average minimum radial circcumference of 85 mm). BP/1/5011 is therefore classified as SC4. The medullary cavity of BP/1/5011 is open and the perimedullary region is poorly preserved. Medium-sized resorption cavities can be seen in the perimedullary region (fig. 4B). These decrease in size and are scattered throughout the section all of the way to the outer cortex. Secondary osteons are dense in the inner cortex and are scattered into the mid-cortex (figs. 4B, 4C and 4D). The tissue is a fibrolamellar complex in the inner and mid-cortex (figs. 4B and 4C). These inner regions show little variation and are a mix of laminar and longitudinal vascular canals (figs. 4B and 4C). The outer cortex has mainly longitudinally-oriented primary osteons with some short circumferential anastomoses in places and the proportion of woven bone has decreased such that this region is comprised of a WPC (fig. 4D). It is well vascularised up to the sub-periosteal surface. Six LAGs including double LAGs are visible throughout the cortex, associated with annuli of parallel-fibred bone (figs. 4D and 4E). The space between them decreases towards the outer cortex. Short Sharpey's fibres are visible throughout the section (fig. 4D).

Ulna

Three ulnae were sampled, the embryonic BP/1/5347a (3.9 mm in circumference, SC1), BP/1/4693 (59mm in circumference, SC3) and NMQR 3964E (64.4 mm in cirumference, SC3).

BP/1/4693 is crushed with parts of the cortex invading the medullary cavity. NMQR3964 is better preserved and has a medullary cavity that contains numerous large trabeculae. Both ulnae have a perimedullary region with large- to medium-sized resorption cavities. In BP/1/4693, scattered secondary osteons are visible along the medial and lateral portions of the inner cortex. In NMQR3964, the lateral side of this region has densely packed secondary osteons (fig. 4F). The bone tissue forms a WPC in bothe specimens (figs. 4G and 4H). There is no variation in vascular arrangement from the inner to outer cortex in either specimen, which consists of large longitudinally-oriented primary osteons with some short anastomoses in places (either circumferential or oblique) (fig. 4G). In BP/1/4693, there appears to be a slight decrease in vascularisation. There are four LAGs visible in BP/1/4693 (with the third one being a quadruple LAG) and six evenly spaced LAGs in NMQR3964 (fig. 4G). These are associated with annulli of parallel-fibred bone in both ulnae (fig. 4H). No Sharpey's fibres are visible in either specimen.

Femora

Only two SC1 femora were available for study (BP/1/5347a and BP/1/5253). These specimens have a minimum circumference of 4.9 mm and 50.5 mm, respectively (2.29% and 23.6% the size of BP/1/4934, respectively). In the larger specimen, the medullary cavity is open and there are no visible trabeculae. The tissue is azonal as there are no identifiable LAGs or annuli. There is no visible change between the inner and mid-cortex (fig. 5A). The bone matrix is a FLC (fig. 5B). The vascularisation displays a mainly laminar arrangement and in some areas a few large longitudinally-oriented primary osteons are present (fig. 5A and 5B). Radiating primary osteons can be seen extending from the medullary cavity to the sub-periosteal surface in some areas of the section (fig. 5A). Given the absence of either growth marks, secondary osteons, resorption cavities or decreased vascularisation towards the periphery this small femur can be considered a juvenile.

There are seven SC2 femora ranging in circumference from 75–105.75 mm (35.05–49.42% the size of BP/1/4934; BP/1/4266 and BP/1/4777, respectively). In all of these specimens, the medullary cavity is open and a few broken trabeculae are present, except in BP/1/4266bB and BP/1/4751B where trabeculae are absent. In most individuals, large- to medium-sized resorption cavities are present in the inner cortex (fig. 5C). These decrease in size and extend to a few scattered cavities in the mid-cortex (e.g. BP/1/ 5238). In general, these specimens contain a rapidly forming WPC, with a dominance of woven bone in the inner cortex indicating the presence of the even faster growing FLC sub-category (fig. 5D). However, the amount of woven bone decreases in the outer cortex, forming the typical WPC (e.g. BP/1/4266 and BP/1/4751). The vascular canals are organised in a laminar arrangement mixed with some longitudinally-oriented primary osteons (fig. 5D and 5E). In some specimens, patches of reticular vascularisation can be seen in the mid- to outer cortex (fig. 5F). The vascularisation in the outermost cortex decreases, but retains the laminar arrangement (e.g. BP/1/5143 mid-cortex).

A few specimens also show signs of remodelling with the presence of secondary osteons in the inner to mid-cortex (e.g. BP/1/5238 and BP/1/5143) (fig. 5C and 5G). All SC2 these specimens have zonal bone tissues with the presence of 5–8 LAGs (the larger specimens do not necessarily have the most LAGs, table 3). These are sometimes associated with annuli of parallel-fibred bone (fig. 5D). These LAGs are often irregularly spaced and do not decrease in spacing towards the sub-periosteal surface except in BP/1/4751 (fig. 11). Double LAGs are present in BP/1/5143 and BP/1/4267 (fig. 5H). No Sharpey's fibres are present in any of the sections.

There are nine SC3 specimens ranging in minimal circumference from 112–160 mm (52.34–74.3% the size of BP/1/4934; BP/1/4693 and BP/1/4928 represent the smallest and largest femora in the SC3 sample, respectively). The tissues in all these specimens form a WPC throughout. The smallest of the specimens shows little variation from the inner to the outer cortex with the vascular arrangement being largely laminar mixed with longitudinally-oriented primary osteons and, in some cases, patches of reticular vascular canals (e.g. BP/1/4693, fig. 6A). BP/1/4693 has a large number of secondary osteons in the inner to mid-cortex (fig. 6B). The larger specimens (such as BP/1/5241, at 67.76% of maximum size) show decreased vascularisation in the outer cortex. Most of these specimens have large to small resorption cavities in the inner cortex, which then extend out into and are scattered throughout the mid-cortex (fig. 6C). Only one specimen lacks resorption cavities (BP/1/5193B). The vascular arrangement in the inner cortex of these specimens is mainly laminar with some patches of reticular and longitudinal canals (e.g. BP/1/5241 and BP/1/5108, see fig. 6C). One specimen, BP/1/5193B, has a small patch of radiating primary osteons in the inner cortex (fig. 7F). The mid-cortex of most SC3 specimens usually exhibits longitudinal and laminar vascular arrangements, with some patches of reticular canals in BP/1/5241and BP/1/5108 (fig. 6E). The outer cortex of SC3 specimens shows a decrease in vascularisation. The vascular organization is still laminar (fig. 6F). The largest specimen in this category, BP/1/4928A (74.77% of maximum size), is very poorly vascularised in the outer cortex in some areas and mainly has longitudinally-oriented primary osteons with a few very short anastomoses (fig. 6G). The specimens in this category have zonal bone tissue with between 4–9 LAGs (the larger specimens do not necessarily have the most LAGs; table 3). These are usually irregularly spaced (fig. 6H) except in BP/1/4693B (52.34% of maximum size), BP/1/5193B (64.65% of maximum size) and BP/1/4928A (74.77% of maximum size) where spacing between the LAGs decreases. Some specimens show annuli of lamellar bone matrix (e.g. BP/1/4998B, fig. 6F).

Two SC4 femora were sampled, BP/1/5397 (estimated femoral circumference of 161.32 mm, 75.38% adult size) and the neotype BP/1/4934B, whose osteohistology has already been described thoroughly in previous studies (Cerda *et al.*, 2017; Barrett *et al.*, 2019).

BP/1/5397 is poorly preserved but shows little change from the inner to the outer cortex. The bone tissue is parallel-fibred and the vascularisation is laminar throughout the cortex (fig. 7A). Medium-sized resorption cavities are present in the inner cortex and smaller ones are scattered throughout the mid-cortex. There is one band of dense secondary remodelling extending from the medullary cavity to the sub-periosteal surface that also contains small resorption cavities throughout (fig. 7B).

BP/1/4934 has resorption cavities in the inner cortex and dense remodelling in the inner to mid-cortex. The bone tissue is WPC to PFB in the outermost cortex and the vascular arrangement is mainly longitudinal. Seven LAGs are present in the section (although many others are inferred to have been lost due to remodelling).

Tibiae

The only SC1 tibia available is BP/1/5347a (3.90 mm in circumference), which was imaged using SRµCT scan data.

There are four SC2 specimens ranging in minimum circumference from 47–80 mm (BP/1/4376 and BP/1/4747 are the smallest and largest, respectively). BP/1/4376 is broken, making the medullary cavity difficult to visualise. There is no bone tissue variation between the inner and outer cortex (fig. 8A). The tissue consists of a WPC (fig. 8B). The vascular arrangement is mainly laminar with small patches of plexiform canals (fig. 8A). There are almost no longitudinally-oriented primary osteons. There is one large annulus of lamellar bone in the middle of the cortex. This is best seen in cross-polarised light (fig. 8C). Sharpey's fibers are present in the mid-cortex.

The medullary cavity is open in the other SC2 specimens. The perimedullary region and inner cortex have numerous medium- to small-sized resorption cavities (fig. 8D). In BP/1/5238, the inner cortex has densely distributed secondary osteons (up to two generations; see fig. 8E). This remodelling makes it difficult to visualise the vascular arrangement. However, the bone tissue appears to be woven with primary osteons, resulting in a WPC with parallel-fibred bone forming an annulus on either side of a LAG (fig. 8F). The mid-cortex in BP/1/5238 contains mainly laminar vascular canals mixed with longitudinally-oriented primary osteons (fig. 8F). The latter have some short, oblique anastomoses connecting them in places. The density of osteocyte lacunae decreases towards the outer mid-cortex. The outer cortex looks slightly less vascularised in BP/1/5238 although it is poorly preserved (fig. 8G and 8H). It consists mainly of longitudinally-oriented primary osteons with some short oblique anastomoses in places. The bone matrix is unclear due to poor preservation although it appears to be a WPC with annuli of parallel-fibred bone associated with a LAG. There is little change in vascularisation in BP/1/4751 (fig. 9A). BP/1/4751C has bands of parallel-fibred bone in the mid- and outer cortex that are associated with LAGs (fig. 9B). The cortex in both BP/1/5238 and BP/1/4751 contains four visible LAGs (table 3) that seem to decrease in spacing (see pdf figure).

The SC3 sample consists of six tibiae that range in diameter from 99.5–138 mm (BP/1/5011 is the largest in the sample). All of the medullary cavities are open. Most of the specimens have medium-to-small resorption cavities in the perimedullary region (except in NMQR 3055, which has none). These decrease in size and are scattered into the mid-cortex (except in BP/1/4928 where they are resticted to the inner cortex). The four smaller SC3 specimens show little bone tissue variation between the inner and outer cortex. The bone is WPC (fig. 9C). The vascular arrangment is mainly laminar with some longitudinally-oriented primary osteons (fig. 9C). BP/1/3055 has secondary osteons in the inner and mid-cortex. The two largest SC3 specimens are extensively secondarily remodelled. BP/1/4928 has densely distributed secondary osteons up to two generations in the inner and mid-cortex (fig. 9D and 9E). The bone is mainly a WPC in these larger specimens, but the outer cortex of BP/1/4928 becomes parallel-fibred (fig. 9F). The outer cortex of BP/1/4928 contains mostly avascular parallel-fibred bone and almost resembles an external fundamental system although there is one row of longitudinally-oriented primary osteons within this region (fig. 9F). In BP/1/5108, vascularisation decreases towards the outer cortex, but still contains laminar canals with some patches of reticular and longitudinally-oriented primary osteons (fig. 9G). Five to 10 irregularly spaced LAGs are visible in the tibiae (fig. 9H, table 3). BP/1/4928B has four LAGs within the outermost, almost avascular, outer cortical region (fig. 11).

Fibulae

Only one SC1 fibula BP/1/5347a (2.66 mm in circumference), is available, imaged using SRµCT scan data.

Two SC3 fibulae were sectioned, ranging in minimum circumference from 67–75 mm (BP/1/4928 and BP/1/4998 are the smallest and largest fibulae, respectively).

Both specimens have open medullary cavities. The perimedullary region of BP/1/4928 has many small resorption cavities. These are also scattered through the mid-cortex. Secondary osteons are also visible in the inner cortex up to the mid-cortex (fig. 10A), up to four generations (fig. 10B). The inner cortical vascularisation and bone matrix are difficult to visualise due to the extensive remodelling, but some circumferentially-arranged primary osteons are visible. The mid-cortex is a WPC with laminar canals (fig. 10C). The outer cortex remains WPC, but is less densely vascularised, although it still displays a laminar arrangement. The sub-periosteal surface is avascular and appears to have an EFS (fig. 10D). Nine irregularly spaced LAGs can be seen (excluding the EFS; an additional six LAGs are in the EFS) (fig. 10E). Annuli of parallel-fibred bone are associated with the LAGs (fig. 10C).

The larger fibula, BP/1/4998, is poorly preserved and the inner cortex is difficult to observe. The bone tissue is a WPC from the inner to the outer cortex (fig. 10F). The vascularisation is a mix of laminar, longitudinal and reticular canals (fig. 10F). Annuli of parallel-fibred bone surround the LAGs (fig. 10F). Vascularisation decreases towards the outer cortex (fig. 10G). The arrangement remains a mix of longitudinally-oriented primary osteons with circumferential anastomoses. Five irregularly spaced LAGs are present, including double LAGs (fig. 10H). No Sharpey's fibres are visible.

Relationship between circumference, cortical thickness, number of LAGs and proportional vascularisation

Correlations between limb bone circumferences and osteohistological variables are weak in *Massospondylus carinatus*. Humeri, femora and tibiae show a poor relationship between log cortical thickness and log circumference (R^2 values of 0.3369, 0.4396 and 0.7158, respectively, when the embryo is excluded to avoid it driving the regression; see fig. 12A–C and Table S4). Similarly, the relationship between the number of visible CGMs and circumference is poorly supported, especially for the femur (R^2 values of 0.4781 for the humerus, 0.1445 for the femur and 0.5745 for the tibia when the embryo is excluded to avoid it driving the regression; see fig. 12D-F and Table S5). Finally, the relationship between the relative area of vascularisation and circumference is extremely poorly correlated (with an R^2 value 0.0743 in the humerus, -0.07073 in the femur and 0.03388 in the tibia respectively, when the embryo is excluded; see fig. 12G-I and Table S6). Finally, although not strongly supported, the relationship between number of humeral LAGs and femoral LAGs shows some significance (with an R^2 value 0.7056, slope of 0.7861, P-value of 0.001; see fig. 12I and Table S7). Similarly, the relationship between the proportional humeral vascularisation and proportional femoral vascularisation also shows some significance (with an R^2 value 0.7874, slope of 0.5023, P-value of 0.01; see fig.11J and Table S7).

Growth curves

An overlapping growth series of femora provides a growth curve for *Massospondylus carinatus* that shows a non-sigmoidal growth trajectory and a retrocalculated maximum age of 20 years old (no LAGs in BP/1/5347 and BP/1/5253, five LAGs in BP/1/4266, nine LAGs in BP/1/5241 and six LAGs in BP/1/4934) (fig. 13A). The overlapping growth series of humeri shows a similar pattern, with a retrocalculated maximum age of 21 years old (no LAGs in BP/1/5347 and BP/1/5253, three LAGs in BP/1/4266, nine LAGs in BP/1/5241 and nine LAGs in BP/1/4934) (fig. 13A).

However, due to the irregular spacing between CGMs and the decoupling between size and number of CGMs, this growth curve could vary depending on which specimens are selected. For example, the longest distances between LAGs in the growth series of femora are as follows: 2049.35 µm in BP/1/4266; 3425.87 µm in BP/1/5241; and 8922.74 µm in BP/1/4934. This leads to a minimum number of three LAGs in BP/1/4266 (cortical thickness of 6065.18 µm), four LAGs in BP/1/5241 (cortical thickness of 14648,61 µm) and two LAGs in BP/1/4934 (cortical thickness of 15892.72 µm), although the first of these overlaps with the last LAG of BP/1/5241 and was excluded. Using these maximum distances, the minimum age at full size of *Massospondylus carinatus* is inferred to be eight years old (fig. 13B).

Conversely, the shortest distance between the LAGs in the femora are 561.24 µm in BP/1/4266; 313.10 µm in BP/1/5241; 247.81 µm in BP/1/4934. The maximum number of LAGs is 11 in BP/1/4266; 47 in BP/1/5241; and 64 in BP/1/4934 although 41 of these overlap with previous specimens and were excluded, bringing the number down to 23 LAGs. Using these minimum distances, the maximum age of *Massospondylus carinatus* at full size is inferred to be 81 years old (fig. 13C).

Discussion

All of the individuals sampled possess limb bones with fast growing zonal bone, as previously reported based on smaller datasets (Chinsamy, 1993; Cerda *et al.*, 2017). Smaller individuals exhibit a highly vascularised WPC, with such high proportions of woven-fibred bone that the bone tissues can be referred to the FLC sub-category of WPC (Prondvai *et al*., 2014; Buffrénil *et al*., 2021). The next smallest post-hatching specimens in the sample, BP/1/5253, does not show any signs of slowed or arrested growth, and in this individuals the cortex is probably recording bone deposited within the first year of growth only.

The second-smallest post-hatchling specimen, BP/1/4376, only includes zeugopodial bones. These exhibit an annulus in the mid-cortex that indicates a temporary decrease in growth rate. In SC3 individuals, the bone tissue is still primarily WPC apart from one tibia (BP/1/4928) that contains parallel-fibred bone in the outer cortex. SC4 bones show a decrease in vascularisation towards the outer cortex and a transition from WPC to parallel-fibred bone tissue.

All bones apart from the two smallest specimens in the sample have CGMs, in the form of LAGs associated, annuli of parallel-fibred or lamellar bone or both. None of the stylopodial bones record an EFS, however, one larger SC3 specimen (BP/1/4928) has an EFS in its tibia and fibula. The femur of BP/1/4928 lacks an EFS but does exhibit a strong decrease in vascularisation in the outer cortex. This, coupled with the annuli present in the radius and tibia of the second smallest specimen, indicates that the zeugopodia record a decrease in growth before the stylopodial bones do, likely because the former grow more slowly. This may be linked to embryonic ossification patterns. It has been recorded that femoral and humeral ossification lags behind that of the tibia/fibula and radius/ulna in archosaur embryos (Rieppel, 1993; Fröbisch, 2008). It has also been found that macroevolutionary changes in limb proportions take place in the stylopod and the autopod, while the trajectory of the zeugopod is more conserved (Young, 2013). This may also explain why the zeugopod ceases to grow sooner than the rest of the long bones. Although none of the stylopodial bones have an EFS, the largest *Massospondylus carinatus* specimen (BP/1/4934) does show signs of slowed growth and being near maximum size (Barrett *et al*., 2019).

The accelerated growth that is thought to characterise earlier ontogenetic stages in growth curves of most animals (Sibly & Brown, 2020), including other dinosaurs, is absent in *Massospondylus carinatus* (figs. 10 and 12D-F) (Erickson, 2005). Contrary to previous hypotheses, the presence of an EFS in the slower growing zeugopodia indicates that *Massospondylus carinatus* did not have indeterminate growth; instead, our results indicate that there are no completely skeletally mature specimens in the sample, consistent with the observation that all vertebrates likely have determinate growth (Woodward, Horner & Farlow, 2011). In our sample, SC1 and SC4 have the smallest sample sizes. This is consistent with the conclusions of Myhrvold (2013), who noted that very immature and very mature individuals are underrepresented in a wide variety of dinosaur clades. This could be due to errors in age estimation methods, or to high mortality rates in mature individuals (due to competition, disease, predation) (Erickson, 2005; Erickson *et al.*, 2006).

The growth curve of LAG number *vs* LAG radius is derived from a series of femora of overlapping circumferences that enabled retro-calculation of the number of LAGs resorbed during remodelling. Based on our femoral growth series, *Massospondylus carinatus* would not have ceased growth before 20 years of age, although it would have been close to its maximum size from 18 years of age (according to BP/1/4934; Barrett *et al*., 2019). This growth trajectory (fig. 16) does not match well with the sigmoidal curve hypothesised for most dinosaur species (Erickson, Rogers & Yerby, 2001; Erickson, 2005; Erickson, 2014). However, the lack of an EFS in any of the femora in the sample affects the shape of this growth curve by removing a potential plateau towards the end of the ontogenetic trajectory.

Given the degree of growth plasticity already reported in *Massospondylus carinatus* (Chapelle *et al*., 2021), where body size is hypothesised to be decoupled from age, it is difficult to assess how informative our femoral series is. There are poor correlations between element circumference (a proxy for body size) and the numbers of LAGs in several elements (fig. 12A-C). We demonstrate that smaller specimens can have a higher number of LAGs than larger individuals, as well as smaller distances between LAGs. Some individuals show similar LAG numbers and spacing across all limb elements (e.g. BP/1/5238 and BP/1/5241), whereas others show a lack of synchroneity (e.g. NMQR 3964 and BP/1/4928) (fig. 10). There are also poor correlations between the degree of vascularisation and element circumference (fig. 12G-I). This supports the earlier observation that *Massospondylus carinatus* exhibits growth plasticity not only in the femur (Chapelle et al., 2021) but in all its limb bones (fig. 12D-F, 11J). The estimated age of 20 years old for the largest known individuals of *Massospondylus carinatus* is slightly less than that reported for other early branching sauropodomorphs. *Plateosaurus trossingensis* has an estimated maximum age of 27 years old (Sander & Klein, 2005), whereas the oldest *Mussaurus patagonicus* specimen has a proposed age of 29–34 years (Cerda *et al* . in press). This agrees with the linear relationship between body mass and life span of poikilothermic animals, with *Plateosaurus trossingensis* and *Mussaurus patagonicus* having a larger body mass than that of *Massospondylus* and therefore expected to have a longer life span (Atanasov, 2005; McPhee *et al.*, 2018). LAG spacing is so variable in *Massospondylus carinatus* that if the maximum distance is used, the minimum age of the largest individuals decreases to 8 years, whereas if the minimum spacing is used, the maximum age increases to 81 (fig. 13A-C). This reiterates the difficulty in correctly determining a growth trajectory for *Massospondylus carinatus*. This type of growth plasticity has been noted in two other early branching sauropodomorphs: *Plateosaurus trossingensis* (Klein & Sander, 2007 and the Science paper) and *Mussaurus patagonicus* (Cerda *et al*., 2021 in press). Both of these taxa show a decoupling between size and estimated age. In addition, *Plateosaurus trossingensis* is hypothesised to reach maximum size (i.e. marked by the presence of an EFS) at different ages. However, the sample includes a mix of stylopodial and zeugopodial bones, which could be obscuring growth patterns due to differences in growth rates between these elements. *Mussaurus patagonicus* shows that some similarly-sized individuals exhibited cyclical growth while others showed continuous growth. This is not the case in *Massospondylus carinatus*, however, as all sampled specimens in SC2 and above (those above 31.95% of maximum body size) show cyclical growth.

Reproductive maturity is usually identified osteohistologically by the transition to slowed growth, either by the decreased spacing of growth marks, or a change in overall tissue type. In our study, there is no evidence for a steep decrease in the growth curve of the larger individuals (fig. 13D–F). Specimens BP/1/3964, BP/1/5193, BP/1/5005, BP/1/4693, BP/1/5241, BP/1/4998, BP/1/5108, BP/1/4928, BP/1/6125, BP/1/5000, BP/1/5011 and BP/1/4934 generally exhibit decreased spacing in LAGs towards the bone periphery, possibly suggesting that these individuals may be reproductively mature (fig. 11). Decreased LAG spacing is more common in the largest specimens (from BP/1/4928 in the above-mentioned list, onward). The tibia of BP/1/5108, the tibia and fibula of BP/1/4928, the humerus of BP/1/6125, radius of BP/1/5011 and humerus and femur of BP/1/4934 were considered adults in this study (based on the degree of secondary remodelling, LAG spacing and number, and the amount of parallel-fibred bone), suggesting that these larger individuals may have been reproductively mature. It is, however, difficult to ascertain an age for the onset of reproductive maturity with confidence.

There are no distinct differences in the growth patterns, amount of vascularisation, or LAG distances between the hindlimb and forelimb of *Massospondylus carinatus* (fig. 12). Multi-element histological studies on *Psittacosaurus lujiatunensis* and *Mussaurus patagonicus* found that the locomotory shift from quadrupedal to bipedal was supported by evidence of faster growth in the humerus than in the femur at early stages of ontogeny. This was also supported by evidence from independent analyses of limb proportional lengths and centre of mass modelling (Zhao *et al.*, 2013) Cerda *et al*. 2022, in press). In *Massospondylus carinatus*, the fore- and hindlimb bones have similar bone tissue textures (i.e., WPC). The amount of vascularisation in the humerus and femur of BP/1/5253, the smallest post-hatching individual is similar (27.11% and 24.90% vascularisation, respectively). This is also the case in the radius and tibia of BP/1/4376, the second smallest individual (21.5% and 19.32% vascularisation, respectively). The vascular arrangement is similar in all four bones (mainly laminar vascularisation with some patches of longitudinal, plexiform and reticular canals). Similarly, in the more mature SC3 individual BP/1/4998, the vascularisation does not differ in any significant way between the humerus, femur, tibia or fibula (20.55%, 22.31%, 15.41% and 25.16% vascularisation, respectively). The regression of humeral vs femoral proportional vascularisation has a slope of 0.5 and an adjusted R^2 value of 0.79 indicating that although the humeri and femora have differing amounts of vascularisation, this proportion remains constant throughout growth history. Finally, in the overlapping growth series, regressions of CGMs number (as a proxy for age) *vs* CGMs radius (as a proxy for size) indicate that the humerus and femur followed similar growth trajectories throughout ontogeny (fig. 13A). Both followed a strongly linear trajectory with adjusted R^2 values of 0.96 and 0.95, respectively. These values do not indicate any noticeable growth pattern changes between the fore- and hindlimb bones.

None of the bones in the sample included medullary bone, an ephemeral type of cancellous bone tissue deposited along the endosteal surface of the medullary cavity as well as in the intertrabecular area of gravid female birds, in which it is resorbed for calcium use in egg and embryo development (Canoville, Schweitzer & Zanno, 2019; de Buffrénil *et al.*, 2021). The absence of medullary bone from our sample does not entail that it is composed exclusively of male individuals but could imply that none of the female individuals sampled were gravid (either due sexual immaturity, or to death outside the reproductive season). Our sample size does not allow for the determination of sexual dimorphism. It is also possible that sauropodomorph dinosaurs did not deposit medullary bone during ovulation as it has yet to be identified with certainty in the clade (de Buffrénil *et al.*, 2021). In this context, neither of the large ontogenetic samples available for *Plateosaurus trossingensis* or *Mussaurus patagonicus* preserve medullary bone.

Conclusion

In recent years, osteohistological analyses of ontogenetic series of non-avian dinosaur taxa have shown more complex growth curves and patterns than previously understood. To better elucidate these, it is required to sample multiple skeletal elements from multiple individuals across a large range of sizes. Our multi-element osteohistological study of *Massospondylus* long bone ranging in size from embryo to adult reveals substantial new information on this early branching sauropodomorph's growth history: 1) the CGMs show growth plasticity in all elements, with a poor correlation between body size and CGMs numbers; 2) the growth trajectory for an individual can vary depending on which limb element is studied; 3) there is no evidence of differential growth rates in forelimb versus hindlimb samples from the same individual, providing further evidence to falsify previously hypothesised ontogenetic postural shifts in *Massospondylus carinatus*. This, along with previous research on related taxa *Plateosaurus trossigensis* and *Mussaurus patagonicus* suggests intraskeletal variation and growth plasticity in Late Triassic and Early Jurassic basal sauropodomorphs. Similar studies are necessary in taxa from different time periods and across the phylogenetic tree to clarify how widespread this was, as well as the driving factors behind it.

Acknowledgements

We thank Sifelani Jirah and Elize Butler for facilitating collections access. Bernhard Zipfel assisted with osteohistological sampling permits. Sekhomotso Gubuza is thanked for providing exceptional help creating and cataloguing the osteohistological sections. KEJC is grateful to Valerie and Charles Rose-Innes for their hospitality in Bloemfontein during data collection. Vincent Fernandez and Paul Tafforeau supervised and conducted scanning at the European Synchrotron Radiation Facility. Martin Sander, Diego Pol and Sterling Nesbitt offered useful discussion during the project. Cecilia Apaldetti, Holly Woodward and Karl Bates are thanked for initial comments and feedback on the study.

References

Atanasov AT. 2005. The linear alometric relationship between total metabolic energy per life span and body mass of poikilothermic animals. *Biosystems* 82:137-142.

Barrett PM, Chapelle KEJ, Staunton CK, Botha J, and Choiniere JN. 2019. Postcranial osteology of the neotype specimen of *Massospondylus carinatus* Owen, 1854 (Dinosauria: Sauropodomorpha) from the upper Elliot Formation of South Africa. *Palaeontolgia Africana* 53:114-178.

Blackburn TJ, Olsen PE, Bowring SA, McLean NM, Kent DV, Puffer J, McHone G, Rasbury ET, and Et-Touhami M. 2013. Zircon U-Pb geochronology links the end-Triassic extinction with the Central Atlantic Magmatic Province. *Science* 340:941-945.

Bordy EM, Abrahams M, Sharman GR, Viglietti PA, Benson RB, McPhee BW, Barrett PM, Sciscio L, Condon D, and Mundil R. 2020. A chronostratigraphic framework for the upper Stormberg Group: Implications for the Triassic-Jurassic boundary in southern Africa. *Earth-Science Reviews*:103120.

Bordy EM, and Catuneanu O. 2002. Sedimentology and palaeontology of upper Karoo aeolian strata (Early Jurassic) in the Tuli Basin, South Africa. *Journal of African Earth Sciences* 35:301-314.

Bordy EM, and Eriksson P. 2015. Lithostratigraphy of the Elliot Formation (Karoo Supergroup), South Africa. *South African Journal of Geology* 118:311-316.

Botha-Brink J, Soares MB, and Martinelli AG. 2018. Osteohistology of Late Triassic prozostrodontian cynodonts from Brazil. *PeerJ* 6:e5029.

Campione NE, Evans DC, Brown CM, and Carrano MT. 2014. Body mass estimation in non-avian bipeds using a theoretical conversion to quadruped stylopodial proportions. *Methods in Ecology and Evolution* 5:913-923.

Canoville A, Schweitzer MH, and Zanno LE. 2019. Systemic distribution of medullary bone in the avian skeleton: ground truthing criteria for the identification of reproductive tissues in extinct Avemetatarsalia. *BMC Evolutionary Biology* 19:1-20.

Catuneanu O, Hancox P, and Rubidge B. 1998. Reciprocal flexural behaviour and contrasting stratigraphies: a new basin development model for the Karoo retroarc foreland system, South Africa. *Basin research* 10:417-440.

Cerda IA, Chinsamy A, Pol D, Apaldetti C, Otero A, Powell JE, and Martínez RN. 2017. Novel insight into the origin of the growth dynamics of sauropod dinosaurs. *PLoS ONE* 12:e0179707.

Cerda IA, Pol D, and Chinsamy A. 2014. Osteohistological insight into the early stages of growth in *Mussaurus patagonicus* (Dinosauria, Sauropodomorpha). *Historical Biology* 26:110-121.

Chapelle KE, Barrett PM, Botha J, and Choiniere JN. 2019a. *Ngwevu intloko*: a new early sauropodomorph dinosaur from the Lower Jurassic Elliot Formation of South Africa and comments on cranial ontogeny in *Massospondylus carinatus*. *PeerJ* 7:e7240.

Chapelle KE, Botha J, and Choiniere JN. 2021. Extreme growth plasticity in the early branching sauropodomorph *Massospondylus carinatus*. *Biology Letters* 17:20200843.

Chapelle KE, and Choiniere JN. 2018. A revised cranial description of *Massospondylus carinatus* Owen (Dinosauria: Sauropodomorpha) based on computed tomographic scans and a review of cranial characters for basal Sauropodomorpha. *PeerJ* 6:e4224. doi: 10.7717/peerj.4224

Chapelle KE, Fernandez V, and Choiniere JN. 2020. Conserved in-ovo cranial ossification sequences of extant saurians allow estimation of embryonic dinosaur developmental stages. *Scientific Reports* 10:1-10.

Chapelle KEJ, Benson RB, Stiegler J, Otero A, Zhao Q, and Choiniere JN. 2019b. A quantitative method for inferring locomotory shifts in amniotes during ontogeny, its application to dinosaurs, and its bearing on the evolution of posture. *Palaeontology* 63:229-242.

Chinsamy A. 1993. Bone histology and growth trajectory of the prosauropod dinosaur *Massospondylus carinatus* Owen. *Modern Geology* 18:319-329.

Cooper MR. 1981. The prosauropod dinosaur *Massospondylus carinatus* Owen from Zimbabwe: its biology, mode of life and phylogenetic significance. *Occasional Papers of the National Museums and Monuments of Rhodesia* 6:690-840.

Cullen TM, Brown CM, Chiba K, Brink KS, Makovicky PJ, and Evans DC. 2021. Growth variability, dimensional scaling, and the interpretation of osteohistological growth data. *Biology Letters* 17:20210383.

Cullen TM, Canale JI, Apesteguía S, Smith ND, Hu D, and Makovicky PJ. 2020. Osteohistological analyses reveal diverse strategies of theropod dinosaur body-size evolution. *Proceedings of the Royal Society B* 287:20202258.

Curry KA. 1999. Ontogenetic histology of Apatosaurus (Dinosauria: Sauropoda): new insights on growth rates and longevity. *Journal of Vertebrate Paleontology* 19:654-665.

de Buffrénil V, de Ricqlès AJ, Zylberberg L, and Padian K. 2021. *Vertebrate Skeletal Histology and Paleohistology*: CRC Press.

Erickson GM. 2005. Assessing dinosaur growth patterns: a microscopic revolution. *Trends in Ecology & Evolution* 20:677-684.

Erickson GM. 2014. On dinosaur growth. *Annual Review of Earth and Planetary Sciences* 42:675-697.

Erickson GM, Currie PJ, Inouye BD, and Winn AA. 2006. Tyrannosaur life tables: an example of nonavian dinosaur population biology. *Science* 313:213-217.

Erickson GM, Curry Rogers K, Varricchio DJ, Norell MA, and Xu X. 2007. Growth patterns in brooding dinosaurs reveals the timing of sexual maturity in non-avian dinosaurs and genesis of the avian condition. *Biol Lett* 3:558-561. 10.1098/rsbl.2007.0254

Erickson GM, Rauhut OWM, Zhou Z, Turner AH, Inouye BD, Hu D, and Norell MA. 2009. Was dinosaurian physiology inherited by birds? Reconciling slow growth in *Archaeopteryx*. *PLoS ONE* 4:1–9.

Erickson GM, Rogers KC, and Yerby SA. 2001. Dinosaur growth patterns and rapid avian growth rates. *Nature* 412:429–433.

Fröbisch NB. 2008. Ossification patterns in the tetrapod limb–conservation and divergence from morphogenetic events. *Biological Reviews* 83:571-600.

Gow CE. 1990. Morphology and growth of the *Massospondylus* braincase (Dinosauria Prosauropoda). *Palaeontologia africana* 27:59-75.

Gow CE, Kitching JW, and Raath MA. 1990. Skulls of the prosauropod dinosaur *Massospondylus carinatus* Owen in the collections of the Bernard Price Institute for Palaeontological Research. *Palaeontologia Africana* 27:45-58.

Horner JR, and Currie PJ. 1994. Embryonic and neonatal morphology and ontogeny of a new species of *Hypacrosaurus* (Ornithischia, Lambeosauridae) from Montana and Alberta. In: Carpenter K, Hirsch KF, and Horner JR, eds. *Dinosaur eggs and babies*. Cambridge: Cambridge University Press, 312–337.
Horner JR, De Ricqlès A, and Padian K. 2000. Long bone histology of the hadrosaurid dinosaur Maiasaura peeblesorum: growth dynamics and physiology based on an ontogenetic series of skeletal elements. *Journal of Vertebrate Paleontology* 20:115-129.
Kitching JW. 1979. Preliminary report on a clutch of six dinosaurian eggs from the Upper Triassic Elliot Formation, Northern Orange Free State. *Palaeontologia africana* 22:41-45.
Kitching JW, and Raath MA. 1984. Fossils from the Elliot and Clarens Formations (Karoo Sequence) of the northeastern Cape, Orange Free State and Lesotho, and a suggested biozonation based on tetrapods. *Palaeontologia Africana* 25:111-125.
Klein N, and Sander M. 2008. Ontogenetic stages in the long bone histology of sauropod dinosaurs. *Paleobiology* 34:247-263.
Klein N, and Sander PM. 2007. Bone histology and growth of the prosauropod dinosaur *Plateosaurus engelhardti* von Meyer, 1837 from the Norian bonebeds of Trossingen (Germany) and Frick (Switzerland). *Special Papers in Palaeontology* 77:169.
Lee AH, and Werning S. 2008. Sexual maturity in growing dinosaurs does not fit reptilian growth models. *Proceedings of the National Academy of Sciences* 105:582-587.
Lehman TM, and Woodward HN. 2008. Modeling growth rates for sauropod dinosaurs. *Paleobiology* 34:264-281.
McPhee BW, Benson RB, Botha-Brink J, Bordy EM, and Choiniere JN. 2018. A giant dinosaur from the earliest Jurassic of South Africa and the transition to quadrupedality in early sauropodomorphs. *Current Biology*.
McPhee BW, Bordy EM, Sciscio L, and Choiniere JN. 2017. The sauropodomorph biostratigraphy of the Elliot Formation of southern Africa: Tracking the evolution of Sauropodomorpha across the Triassic–Jurassic boundary. *Acta Palaeontologica Polonica* 62:441-465.
Munyikwa D. 1997. Faunal analysis of Karoo-aged sediments in the northern Limpopo Valley, Zimbabwe. *Arnoldia Zimbabwe* 10:129-139.
Myhrvold NP. 2013. Revisiting the estimation of dinosaur growth rates. *PLoS ONE* 8:e81917.
Neenan JM, Chapelle KE, Fernandez V, and Choiniere JN. 2018. Ontogeny of the *Massospondylus* labyrinth: implications for locomotory shifts in a basal sauropodomorph dinosaur. *Palaeontology* 62:1–11.
Reisz RR, Huang TD, Roberts EM, Peng S, Sullivan C, Stein K, LeBlanc AR, Shieh D, Chang R, Chiang C, Yang C, and Zhong S. 2013. Embryology of Early Jurassic dinosaur from China with evidence of preserved organic remains. *Nature* 496:210-214. 10.1038/nature11978
Reisz RR, Scott D, Sues H-D, Evans DC, and Raath MA. 2005. Embryos of an Early Jurassic prosauropod dinosaur and their evolutionary significance. *Science* 309:761–764.
Rieppel O. 1993. Studies on skeleton formation in reptiles. V. Patterns of ossification in the skeleton of Alligator mississippiensis Daudin (Reptilia, Crocodylia). *Zoological Journal of the Linnean Society* 109:301-325.
Rogers RR, Rogers KC, Munyikwa D, Terry RC, and Singer BS. 2004. Sedimentology and taphonomy of the upper Karoo-equivalent Mpandi Formation in the Tuli Basin of Zimbabwe, with a new 40Ar/39Ar age for the Tuli basalts. *Journal of African Earth Sciences* 40:147-161.
Sander PM. 1999. Life history of Tendaguru sauropods as inferred from long bone histology. *Fossil Record* 2:103-112.
Sander PM, and Klein N. 2005. Developmental plasticity in the life history of a prosauropod dinosaur. *Science* 310:1800-1802.

Schneider CA, Rasband WS, and Eliceiri KW. 2012. NIH Image to ImageJ: 25 years of image analysis. *Nature methods* 9:671.
Sibly R, and Brown J. 2020. Toward a physiological explanation of juvenile growth curves. *Journal of Zoology* 311:286-290.
Skutschas PP, Morozov SS, Averianov AO, Leshchinskiy SV, Ivantsov SV, Fayngerts AV, Feofanova OA, Vladimirova ON, and Slobodin DA. 2021. Femoral histology and growth patterns of the ceratopsian dinosaur Psittacosaurus sibiricus from the Early Cretaceous of Western Siberia. *Acta Palaeontologica Polonica* 66:437-447.
Stein K, and Prondvai E. 2014. Rethinking the nature of fibrolamellar bone: an integrative biological revision of sauropod plexiform bone formation. *Biol Rev Camb Philos Soc* 89:24-47. 10.1111/brv.12041
Stein M, Hayashi S, and Sander PM. 2013. Long bone histology and growth patterns in ankylosaurs: implications for life history and evolution. *PLoS ONE* 8:e68590.
Sues H-D, Reisz RR, Hinic S, and Raath MA. 2004. On the skull of *Massospondylus carinatus* Owen, 1854 (Dinosauria: Sauropodomorpha) from the Elliot and Clarens formations (Lower Jurassic) of South Africa. *Annals of Carnegie Museum* 73:239-257.
Team R. 2016. RStudio: Integrated Development for R. RStudio, Inc., Boston, MA.
Viglietti P, McPhee B, Bordy E, Sciscio L, Barrett P, Benson R, Wills S, Chapelle K, Dollman K, and Mdekazi C. 2020. Biostratigraphy of the *Massospondylus* Assemblage Zone (Stormberg Group, Karoo Supergroup), South Africa. *South African Journal of Geology* 123:249-262.
Werning S. 2012. The ontogenetic osteohistology of Tenontosaurus tilletti. *PLoS ONE* 7:e33539.
Woodward HN, Horner JR, and Farlow JO. 2011. Osteohistological evidence for determinate growth in the American alligator. *Journal of Herpetology* 45:339-343.
Woodward HN, Horner JR, and Farlow JO. 2014. Quantification of intraskeletal histovariability in *Alligator mississippiensis* and implications for vertebrate osteohistology. *PeerJ* 2:e422.
Young NM. 2013. Macroevolutionary diversity of amniote limb proportions predicted by developmental interactions. *Journal of Experimental Zoology Part B: Molecular and Developmental Evolution* 320:420-427.
Zhao Q, Benton MJ, Sullivan C, Martin Sander P, and Xu X. 2013. Histology and postural change during the growth of the ceratopsian dinosaur Psittacosaurus lujiatunensis. *Nat Commun* 4:2079. 10.1038/ncomms3079

Table 1 (on next page)

Table 1: Minimum circumferences of the complete dataset for analysis.

Missing femoral circumferences were estimated using femoral to humeral regressions (in yellow) and femoral to tibial regressions (in orange) (see text for details). %size based on estimated femoral circumferences (see text). Asterisks indicate historical thin-sections from Chinsamy (1993). Daggers indicate circumferences measured from thin-sections. Tilde symbols indicate approximate circumferences due to poor preservation. Double daggers indicate sections too damaged to measure. Abbreviations: C, circumference; Diag, diagenetic; Fem, femur; Fib, fibula; Hum, humerus; Rad, radius; Remod, remodelled; SC, size class; Tib, tibia; Uln, ulna.

Specimen number	HumC (mm)	RadC (mm)	UlnC (mm)	FemC (mm)	TibC (mm)	FibC (mm)	Estimated FemC (mm)	%Size	SC
BP/1/5347a	3.61	1.88	3.90	4.9	3.90	2.70		2.29	SC1
BP/1/5253*	29.5			50.5				23.60	SC1
BP/1/4376		21.5			~47		3668.15	31.85	SC2
BP/1/4266b*	46			75				35.05	SC2
BP/1/5238				81	68			37.85	SC2
BP/1/5143*				83				38.79	SC2
BP/1/4267				85				39.72	SC2
BP/1/4751	52			93	57.89†			43.46	SC2
BP/1/4747*				95	80			44.39	SC2
BP/1/4777*				105.75†				49.42	SC2
BP/1/4693*			~59	112				52.34	SC3
NMQR3055	72			114	99.54			53.27	SC3
NMQR3964	78		64.6				125.26	58.53	SC3
BP/1/5108				145‡	107.23†		131.51	61.45	SC3
BP/1/4999	85				~130		135.45	63.30	SC3
BP/1/5193	87			100‡			138.35	64.65	SC3
BP/1/4860	84			143	107			66.82	SC3
BP/1/5241*	89			145				67.76	SC3
BP/1/4998	100			145	111	75		67.76	SC3
BP/1/5005	101						158.46	74.05	SC3
BP/1/4861*				159				74.30	SC3
BP/1/4928				160	138	67		74.77	SC3
BP/1/5397	103			100‡			161.32	75.38	SC4
BP/1/6125	115						178.33	83.33	SC4
BP/1/5000	131						200.77	93.82	SC4
BP/1/4934	141			~214				100	SC4
BP/1/5011		81							

Table 2(on next page)

Table 2: Fore limb long bone CGM numbers and proportional vascularization with relative size (based on Table 1).

Tilde symbols indicate approximate circumferences due to poor preservation. Abbreviations: CGMs; Cyclical Growth Marks; Diag, diagenetic; Hum, humerus; No, number; Rad, radius; Remod, remodelled; SC, size class; Uln, Ulna; Vasc, vascularisation.

Specimen number	%Size	SC	Hum No of CGMs	Hum % Cortex	Hum %Vasc	Rad No of CGMs	Rad % Cortex	Rad %Vasc	Uln No of CGMs	Uln % Cortex	Uln %Vasc
BP/1/5347a	2.29	SC1	0	47.04		0	60.61		0	58	
BP/1/5253*	23.60	SC1	0	49.63	27.11						
BP/1/4376	31.85	SC2				1	46.05	19.32			
BP/1/4266b *	35.05	SC2	3	54.56	Diag						
BP/1/4751	43.46	SC2	5	45.21	18.83						
BP/1/4693*	52.34	SC3							4	?	12.59
NMQR3055	53.27	SC3	4	53.20	18.02						
NMQR3964	58.53	SC3	6	36.23	Diag				6	72.45	Diag
BP/1/4999	63.30	SC3	6	47.19	28.91						
BP/1/5193	64.65	SC3	6?	46.98	23.70						
BP/1/4860	66.82	SC3	6-8	57.03	Diag						
BP/1/5241*	67.76	SC3	8	48.51	9.32						
BP/1/4998	67.76	SC3	3	22.26	20.55						
BP/1/5005	74.05	SC3	13	50.67	10.54						
BP/1/5397	75.38	SC4	5	53.16	18.22						
BP/1/6125	83.33	SC4	10	54.84	16.43						
BP/1/5000	93.82	SC4	7-8	33.52	Remod						
BP/1/4934	100	SC4	10	?	Remod						
BP/1/5011		SC4				6	59.25	6.80			

1

Table 3 (on next page)

Table 3: Hind limb long bone CGM numbers and proportional vascularization with relative size (based on Table 1).

Tilde symbols indicate approximate circumferences due to poor preservation. Abbreviations: CGMs; Cyclical Growth Marks; Diag, diagenetic; Fem, femur; Fib, fibula; No, number; Remod, remodelled; SC, size class; Tib, tibia; Vasc, vascularisation.

Specimen number	%Size	SC	Fem No of CGMs	Fem % Cortex	Fem %Vasc	Tib No of CGMs	Tib % Cortex	Tib %Vasc	Fib No of CGMs	Fib % Cortex	Fib %Vasc
BP/1/5347a	2.29	SC1	0	45.45		0	62		0	59.50	
BP/1/5253*	23.60	SC1	0	46.29	24.9						
BP/1/4376	31.85	SC2				1	39.03	21.47			
BP/1/4266b*	35.05	SC2	5	44.64	Diag						
BP/1/5238	37.85	SC2	5	50.63	10.17	4	55.35	9.6			
BP/1/5143*	38.79	SC2	8	53.11	5.80						
BP/1/4267	39.72	SC2	5	47	11.82						
BP/1/4751	43.46	SC2	5	39.62	23.15	4	52.10	26.19			
BP/1/4747*	44.39	SC2	4	36.16	16.81						
BP/1/4777*	49.42	SC2	8	46.04	8.11						
BP/1/4693*	52.34	SC3	8	54.81	9.97						
NMQR3055	53.27	SC3	6	47.15	22.60	5?	60.63	24.03			
BP/1/5108	61.45	SC3	9	39.24	Diag	10?	55.64	25.08			
BP/1/4999	63.30	SC3									
BP/1/5193	64.65	SC3	6	26.05	26.97						
BP/1/4860	66.82	SC3	4	?	Diag	5	43.90	10.28			
BP/1/5241*	67.76	SC3	9	50.72	17.02						
BP/1/4998	67.76	SC3	4	15.40	22.31	5-6	37.69	15.41	6	46.70	25.16
BP/1/4861*	74.30	SC3	9	47.46	Remod						
BP/1/4928	74.77	SC3	7	67.21	Diag	8	71.94	8.00	9	53.84	Remod
BP/1/5397	75.38	SC4	5	42.05	Diag						
BP/1/4934	100	SC4	214	?	Remod						

1

Table 4(on next page)

Table 4: Osteohistological nomenclature, descriptions and abbreviations used (from de Buffrénil et al., 2021).

Morphology	Description	Abbreviation
Annulus	Any cyclical modification in the matrix structure of primary cortices, indicating a temporary decrease in growth rate	N/A
Line of Arrested Growth	Dark lines that can be traced around the cortex, formed by a temporary cessation in skeletal growth	LAG
Sharpey's fibers	In periosteal deposits, thick bundles (6–7 µm in average diameter) of varying lengths, representing fibres that anchor a tissue or an organ external to the bone	SF
External Fundamental Systems	Layers of parallel-fibered or lamellar tissues, located along the outer margins of periosteal cortices, indicating a steep decrease in subperiosteal accretion rate that occurs at the end of somatic growth	EFS
Longitudinal vascular canals	Simple canals or primary osteons, can be composed of longitudinal canals (i.e., canals oriented parallel to the long axis of the bone) that can be united or not by transverse anastomoses. Longitudinal canals can have a random distribution, or be distributed in radial or circular rows	N/A
Oblique vascular arrangement	Nonlongitudinal canals, variable angle compared to the bone's sagittal axis	N/A
Reticular vascular arrangement	Nonlongitudinal canals, form a random network with no dominant orientation	N/A
Radiating vascular arrangement	Nonlongitudinal canals, extend approximately in parallel with the radii of a long bone cross section	N/A
Plexiform vascular arrangement	Nonlongitudinal canals, arranged circumferentially around the bone (i.e., parallel to the outer contour of the cortex) and forming parallel strata united by numerous radial anastomoses	N/A
Laminar vascular arrangement	Nonlongitudinal canals, similar orientation as plexiform arrangement but with fewer anastomoses	N/A
Woven-Fibered Collagen Networks	Intercellular matrix, formed by static osteogenesis, characterised by fibers and fiber bundles with no preferential orientation, formed by randomly oriented osteoblasts	WFM
Parallel-Fibered Matrix	Primary compact tissue, characterised by parallel-fibered matrix with spindle-like or flat osteocyte lacunae oriented parallel to the general direction of the collagen fibers or at least evenly distributed; the collagen fibers are parallel to the outer contours of the bones	PFM
Lamellar Matrix	Intercellular matrix, formed by dynamic osteogenesis, characterised by collagen fibers that are not all oriented in a unique, exclusive direction but are rather arranged in a series of stacked, well-differentiated lamellae	LM
Woven-Fibered Bone Tissue	Primary compact tissue, characterised by woven-fibered matrix with large, multipolar osteocyte lacunae randomly	WFB

	oriented within the matrix	
Parallel-Fibered Bone Tissue	Primary compact tissue, characterised by parallel-fibered matrix with spindle-like or flat osteocyte lacunae oriented parallel to the general direction of the collagen fibres; the latter are parallel to the outer contours of the bones	PFB
Lamellar Bone Tissue	Primary compact tissue, characterised by a parallel-fibered matrix, with spindle-like or flat osteocyte lacunae oriented parallel to the general direction of the collagen fibres, with occurrence of lamellae within the matrix of the lamellar tissue	LB
Woven-Parallel Complexes	Previously known as fibrolamellar bone. Primary periosteal tissues with woven-fibered component and lamellar component in the form of primary osteons. The fibrolamellar complex (FLC) is a sub-category of WPC and is identified by the notably high proportion of woven bone over parallel-fibered bone	WPC
Medullary bone	Highly vascularized, mostly woven, endosteally-derived tissue that develops within large bone cavities containing marrow (Canoville 2019)	MB

1

Figure 1

Figure 1: SC1 and SC2 humeral osteohistology.

A, overview in normal light of the cortex of SC1 BP/1/5253, scale bar = 500 µm. B, high magnification in normal light of the inner cortex of SC1 BP/1/5253 showing FLC, scale bar = 250µm. C, overview in normal light of SC2 BP/1/4266 showing resorption cavities, scale bar = 500µm. D, high magnification in normal light of the inner cortex of the SC2 BP/1/4751 showing resorption cavities, plexiform vascular arrangement and FLC, scale bar = 1000µm. E, high magnification in normal light the mid-cortex of the SC2 BP/1/4751 showing WPC with an annulus of parallel-fibred bone associated with a LAG and increase in PFB towards the outer cortex, scale bar = 500µm. F, high magnification in normal light of the outer cortex of the SC2 BP/1/4751 showing a decrease in vascularization, scale bar = 500µm. G, high magnification in cross-polarised light of the outer cortex of the SC2 BP/1/4751 showing annuli of parallel-fibred bone associated with the LAGs, scale bar = 250µm. H, overview in normal light of the cortex of the SC2 BP/1/4751 showing LAG distribution and transition from WPC to PFB, scale bar = 500µm. Black and white arrowheads indicate single LAGs; yellow arrowheads indicate triple LAGs. Abbreviations: MC, medullary cavity; PFB, parallel-fibred bone; RC, resorption cavity; WPC, woven-parallel complex.

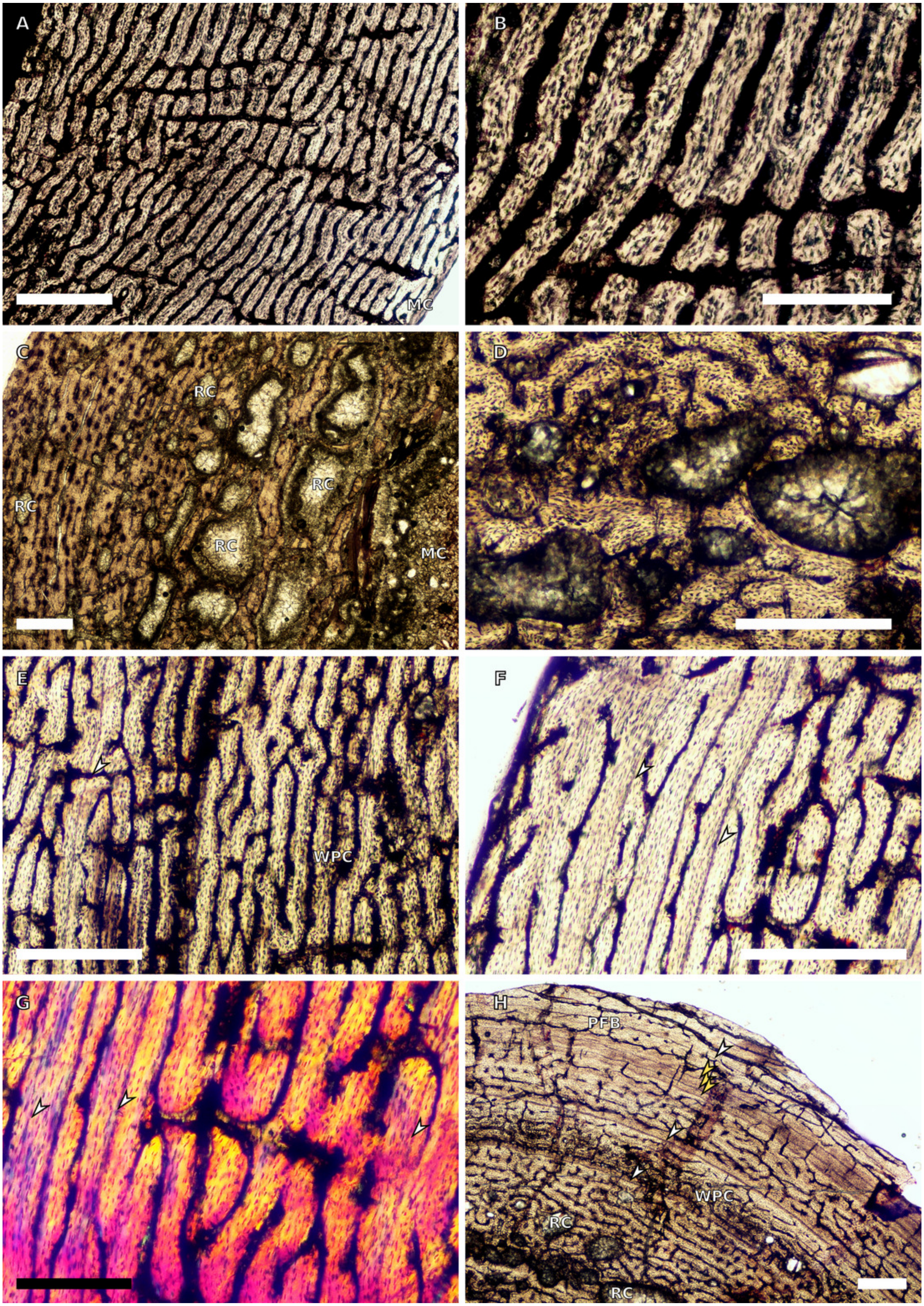
A
MC
B
C
RC
RC
RC
RC
MC
D
E
WPC
F
G
H
PFB
WPC
RC
RC

Figure 2

Figure 2: SC3 humeral osteohistology.

A, overview in normal light of the cortex of BP/1/4860A showing a plexiform vascular arrangement in the inner and mid-cortex possibly exaggerated by diagenesis, scale bar = 500 µm. B, high magnification in normal light of the inner cortex of BP/1/5005 showing secondary osteons, scale bar = 500 µm. C, high magnification in normal light of the mid-cortex of BP/1/5005 showing a mix of laminar and plexiform vascular arrangements, scale bar = 500 µm. D, high magnification in normal light of the outer cortex of BP/1/4998A showing a WPC, scale bar = 250 µm. E, high magnification in normal light of the outer cortex of BP/1/5005 showing a WPC with annuli of parallel-fibred bone associated with LAGs, scale bar = 250 µm. F, overview in normal light of the cortex of BP/1/5005 showing LAG distribution, scale bar = 1000µm. G, high magnification in cross-polarised light of the outer cortex of BP/1/5241A showing annuli of lamellar bone associated with LAGs, scale bar = 250 µm. H, high magnification in cross-polarised light of outer cortex of BP/1/5241A showing Sharpey's fibres, scale bar = 500 µm. White arrowheads indicate single LAGs; yellow arrowheads indicate double LAGs. Abbreviations: LB, lamellar bone; LV, laminar vascular arrangement; MC, medullary cavity; RC, resorption cavity; PFB, parallel-fibred bone; PV, plexiform vascular arrangement; SF, Sharpey's fibres; SO, secondary osteon; WPC, woven-parallel complex.

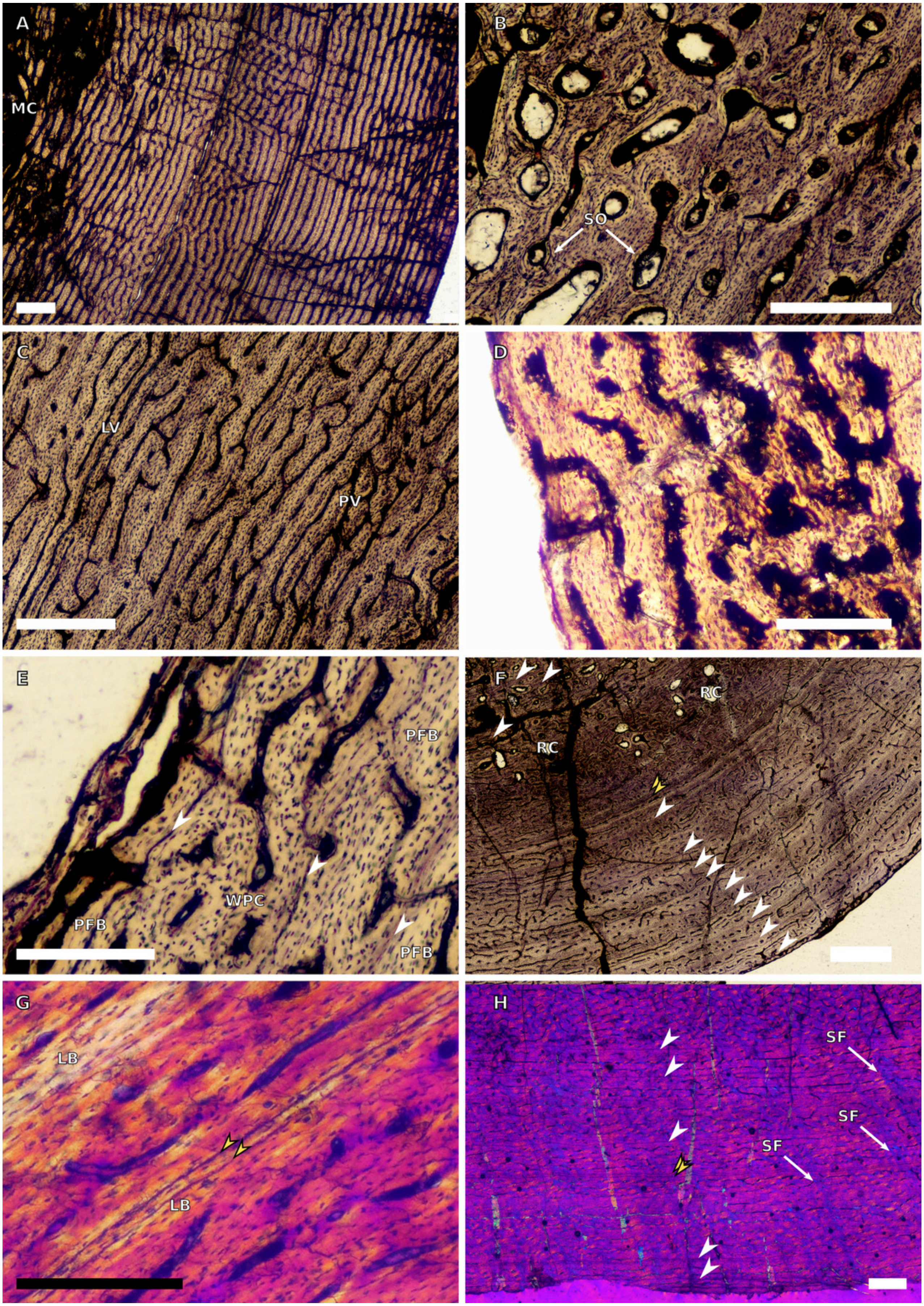
A
MC
B
SO
C
LV
PV
D
E
PFB
WPC
PFB
PFB
F
RC
RC
G
LB
LB
H
SF
SF
SF

Figure 3

Figure 3: SC4 humeral osteohistology.

A, high magnification in normal light of the perimedullary region of BP/1/5397 showing resorption cavities and secondary osteons, scale bar = 500 µm. B, high magnification in normal light of the inner cortex of BP/1/5297 showing longitudinal and laminar arrangement of canals, scale bar = 500 µm. C, high magnification in normal light of the inner cortex of BP/1/6125 showing primary and secondary osteons, scale bar = 500 µm. D, high magnification in normal light of the mid-cortex of BP/1/6125 showing a plexiform vascular arrangement, scale bar = 500 µm. E, high magnification in cross-polarised light of the outer cortex of BP/1/6125 showing a WPC with decreasing vascularization and annuli of lamellar bone associated with LAGs, scale bar = 500 µm. F, overview in normal light of the cortex of BP/1/6125 showing the LAG distribution, scale bar = 1000 µm. White arrowheads indicate single LAGs; yellow arrowheads indicate double LAGs. Abbreviations: MC, medullary cavity; PFB, parallel-fibred bone; PO, primary osteon; RC, resorption cavity; SO, secondary osteon.

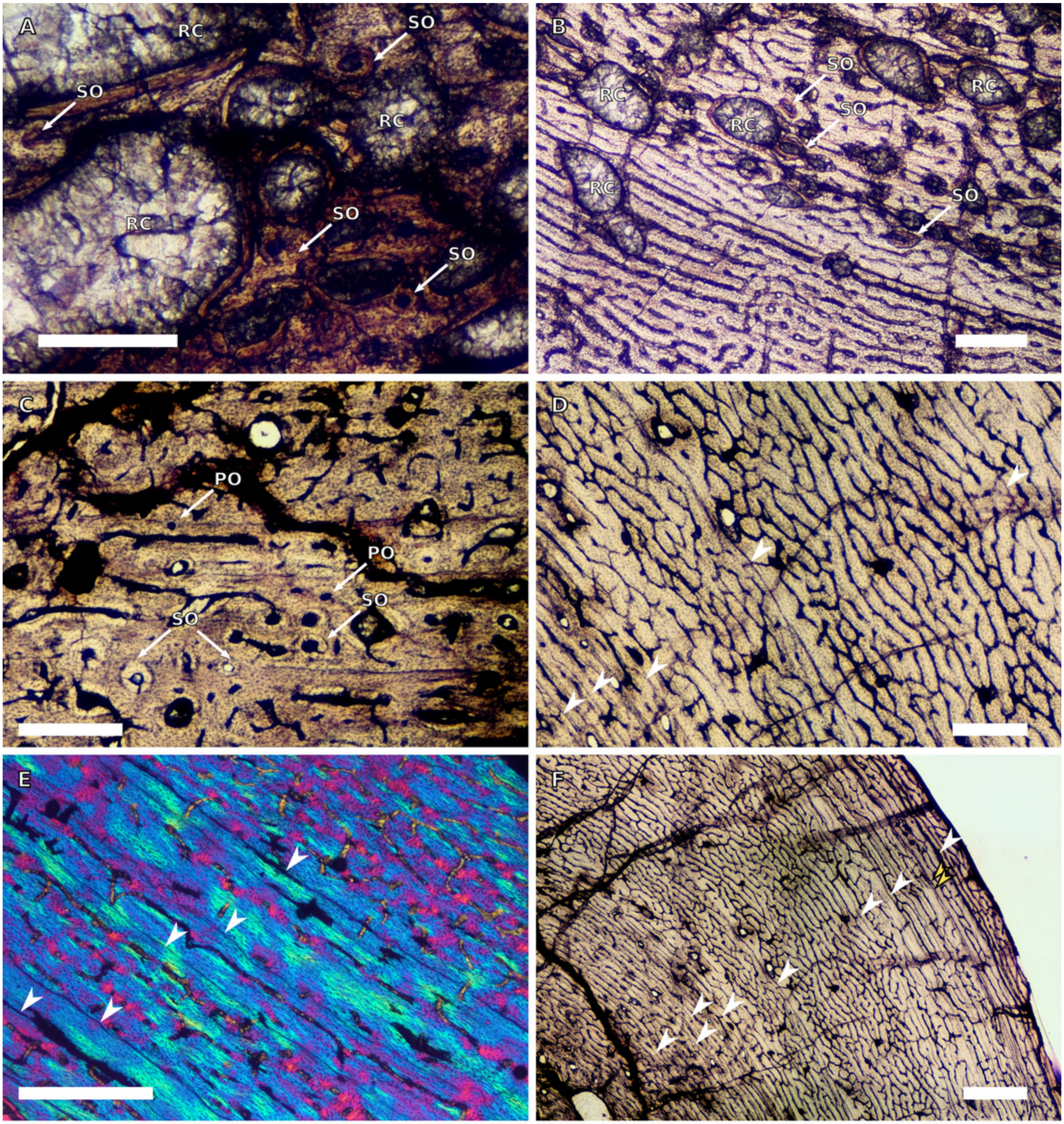
A
RC
SO
SO
RC
RC
SO
SO
B
SO
SO
RC
RC
RC
RC
SO
C
PO
PO
SO
SO
D
E
F

Figure 4

Figure 4: Ulna and radius osteohistology.

A, overview in normal light of the cortex of the BP/1/4376A radius (SC2) showing Sharpey's fibres, scale bar = 250 µm. B, high magnification in normal light of the radial inner cortex of BP/1/5011A (SC4) showing a WPC and an annulus of parallel-fibred bone associated with a LAG as well as secondary osteons, scale bar= 500 µm. C, high magnification in normal light of the radial mid-cortex of BP/1/5011 (SC4) showing a WPC and LAGs as well as secondary osteons, scale bar= 500 µm. D, high magnification in normal light of the radial outer cortex of BP/1/5011 (SC4) showing Sharpey's fibres, longitudinal canals (some of which are simple) and secondary osteons, scale bar = 500 µm. E, overview in normal light of the radial cortex of BP/1/5011 (SC4) showing LAG distribution, scale bar = 1000 µm. F, high magnification in normal light of the inner cortex of the ulna of NMQR 3964E (SC3) showing densely distributed secondary osteons, scale bar = 500 µm. G, high magnification in normal light of the cortex of the ulna of NMQR 3964E (SC3) showing LAG distribution and large longitudinal primary osteons throughout the cortex, scale bar = 500 µm. H, close–up in normal light of the mid-cortex of the ulna of NMQR 3964E (SC3) showing a WPC, PFB and a LAG, scale bar = 250 µm. White arrowheads indicate single LAGs; yellow arrowheads indicate double LAGs. Abbreviations: MC, medullary cavity; PFB, parallel-fibred bone; RC, resorption cavity; SF, Sharpey's fibres; SO, secondary osteon; WB, woven bone; WPC, woven-parallel complex.

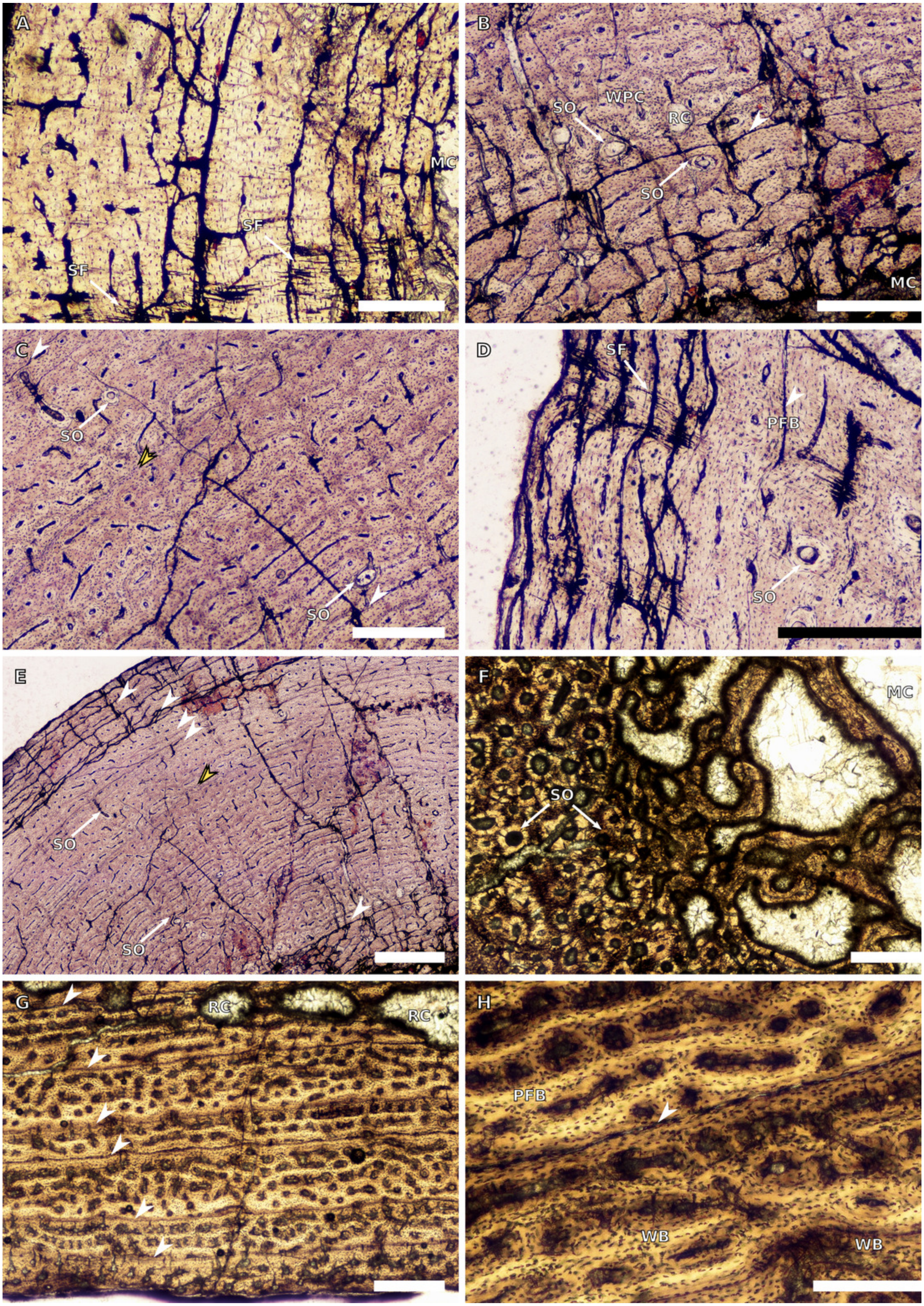
A
SF
SF
MC
B
SO
WPC
RC
SO
MC
C
SO
SO
D
SF
PFB
SO
E
SO
SO
F
MC
SO
G
RC
RC
H
PFB
WB
WB

Figure 5

Figure 5: SC1 and SC2 femoral osteohistology.

A, overview in normal light of the cortex of BP/1/5253B (SC1) showing little variation from the inner to outer cortex, scale bar = 500 µm. B, high magnification in cross-polarised light of the cortex of BP/1/5253B (SC1) showing a fibrolamellar complex with laminar vascular arrangement, scale bar = 200 µm. C, high magnification in normal light of the inner cortex of BP/1/5143 (SC2) showing secondary osteons and resorption cavities, scale bar = 500 µm. D, high magnification in normal light of the mid-cortex in BP/1/4267 (SC2) showing a fibrolamellar complex with annuli of parallel-fibred bone, scale bar = 500 µm. E, high magnification in normal light of the outer cortex of BP/1/4267 (SC2) showing a WPC, scale bar= 250 µm. F, high magnification in normal light of the mid- to outer cortex of BP/1/5143 (SC2) showing a reticular vascular arrangement, scale bar = 250 µm. G, close–up in normal light of the inner cortex of BP/1/5238 (SC2) showing secondary remodelling, scale bar= 500 µm. H, high magnification in normal light of the outer cortex of BP/1/5143 (SC2) showing a decrease in vascularization and overall transition to PFB, scale bar = 500 µm. White arrowheads indicate single LAGs; yellow arrowheads indicate double and triple LAGs. Abbreviations: FLC, fibrolamellar complex; MC, medullary cavity; PFB, parallel-fibred bone; RC, resorption cavity; SO, secondary osteon; WPC, woven-parallel complex.

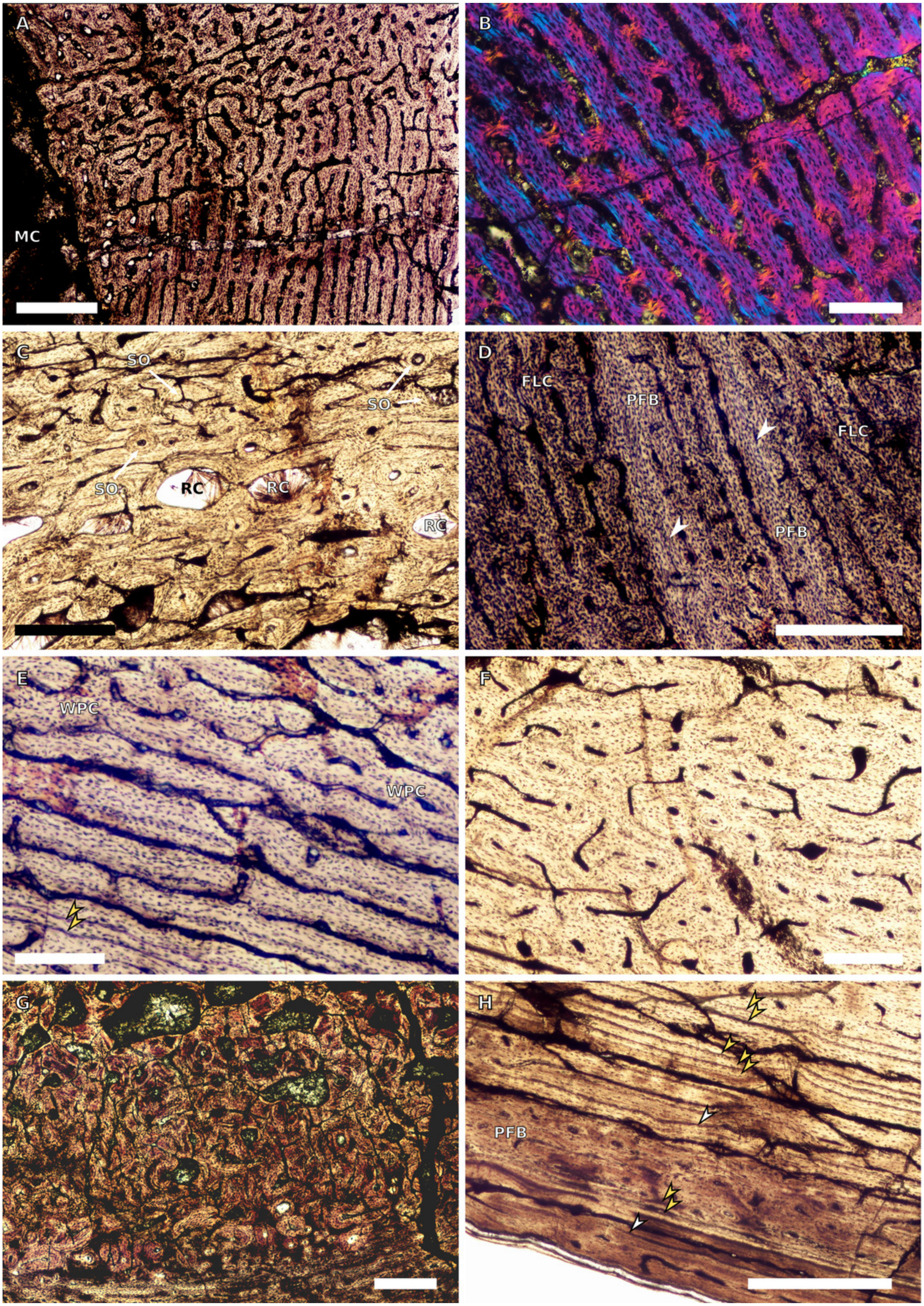
A
MC
B
C
SO
SO
SO
RC
RC
RC
D
FLC
PFB
FLC
PFB
E
WPC
WPC
F
G
H
PFB

Figure 6

Figure 6: SC3 femoral osteohistology.

A, overview in normal light of the cortex of BP/1/4693B showing little bone tissue variation between the inner and outer cortex, scale bar = 1000 µm. B, high magnification in normal light of the mid-cortex of BP/1/4693B showing secondary osteons, scale bar = 250 µm. C, high magnification in normal light of BP/1/5241 inner cortex showing a mainly laminar vascular arrangement with some patches of plexiform canals, scale bar = 1000 µm. D, high magnification in cross-polarised light of BP/1/5241 mid-cortex showing a WPC with a plexiform vascular arrangement, scale bar = 300 µm. E, high magnification in normal light of the outer cortex of BP/1/5241 showing a mix of laminar and longitudinal vascular arrangements, scale bar= 500 µm. F, high magnification in normal light of the outer cortex of BP/1/4998B showing a laminar arrangement and annuli of lamellar bone , scale bar= 250 µm. G, high magnification in normal light of the outer cortex of BP/1/4928A showing decreased vascularization, scale bar = 500 µm. H, overview in normal light of BP/1/5241 showing LAG spacing, scale bar = 1000 µm. White arrowheads indicate single LAGs; yellow arrowheads indicate double and triple LAGs. Abbreviations: LB, lamellar bone; LV, laminar vascularization; MC, medullary cavity; PFB, parallel-fibred bone; PV, plexiform vascularization; RC, resorption cavity; SO, secondary osteon.

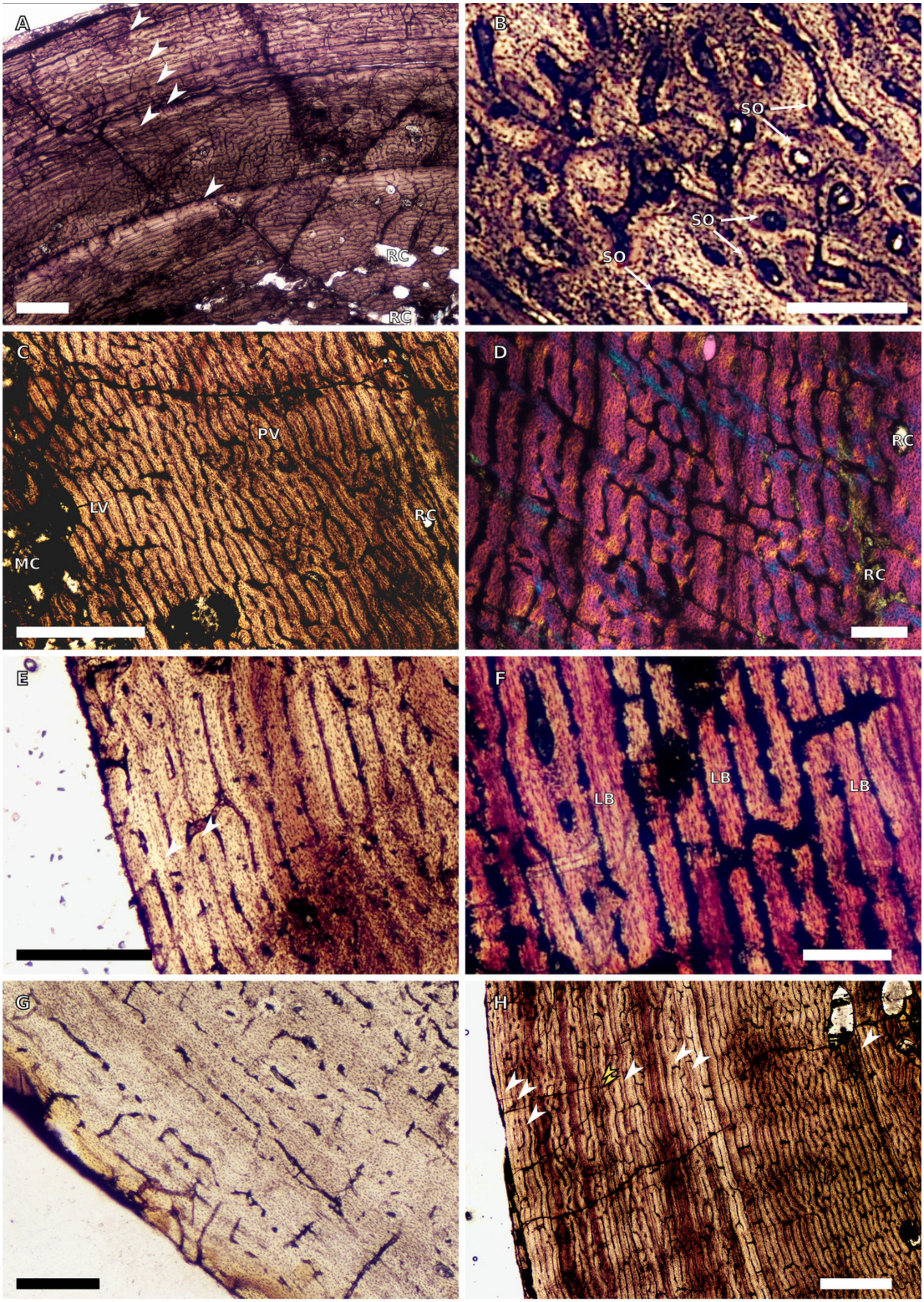
A
RC
RC
B
SO
SO
SO
C
PV
LV
RC
MC
D
RC
RC
E
F
LB
LB
LB
G
H

Figure 7

Figure 7: SC4 femoral histology.

A, overview in normal light of the cortex of BP/1/5397 showing little bone tissue variation between the inner and outer cortex, scale bar = 1000 µm. B, high magnification in normal light of the mid-cortex of BP/1/5397 showing heavy secondary remodelling, scale bar = 500 µm. Abbreviations: MC, medullary cavity; RC, resorption cavity.

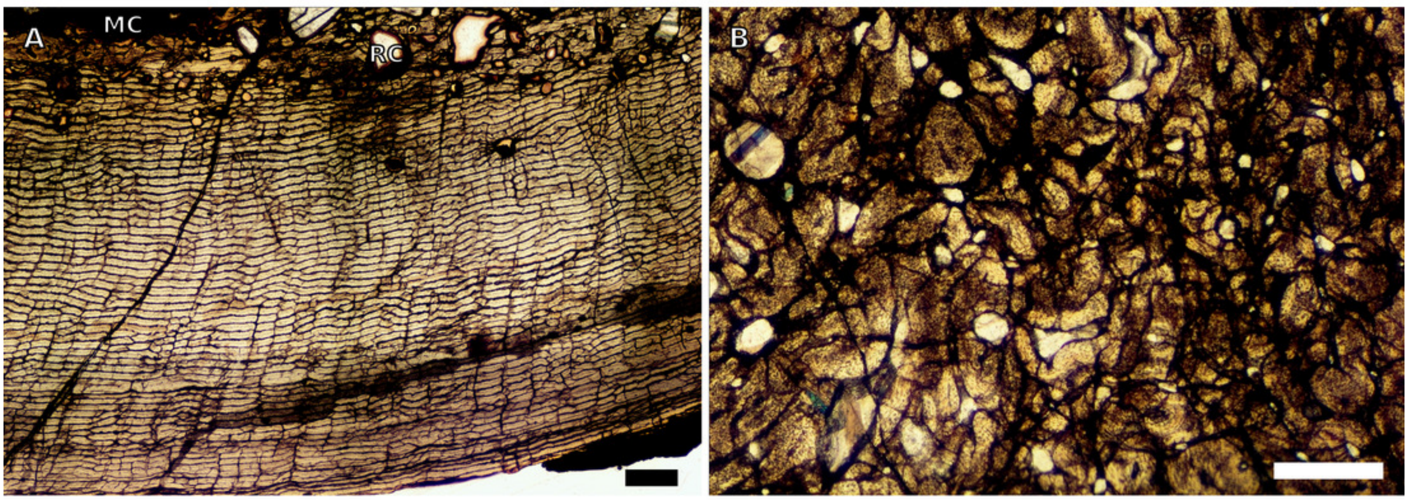

Figure 8

Figure 8: SC2 tibial osteohistology.

A, high magnification in cross-polarised light of the mid- to outer cortex in the smallest SC2 tibia, BP/1/4376B, showing variation between plexiform and laminar vascular arrangements, scale bar = 300 µm. B, high magnification in normal light of the mid-cortex of BP/1/4376B showing WPC with an annulus of parallel-fibred bone and Sharpey's fibres, scale bar = 500 µm. C, high magnification in cross polarised-light of the mid-cortex of BP/1/4376B showing a annulus of parallel-fibred bone, scale bar = 250 µm. D, high magnification in normal light of BP/1/5238 inner cortex showing large resorption cavities, scale bar = 500 µm. E, close–up in normal light of the inner cortex of BP/1/5238 showing secondary osteons up to two generations, scale bar= 250 µm. F, high magnification in normal light of the inner to mid-cortex of BP/1/5238 showing WPC with an annulus as well as a laminar vascular arrangement, scale bar= 250 µm. G, high magnification in normal light of the outer cortex of BP/1/5238 showing a decrease in vascularization and an annulus of parallel-fibred bone, scale bar = 250 µm. H, overview in cross-polarised light of the outer cortex of BP/1/5238 showing LAG distribution, scale bar = 500 µm. White arrowheads indicate annuli and single LAGs. Abbreviations: LV, laminar vascularization; MC, medullary cavity; PFB, parallel-fibred bone; PV, plexiform vascularization; RC, resorption cavity; SO, secondary osteon; WPC, woven-parallel complex.

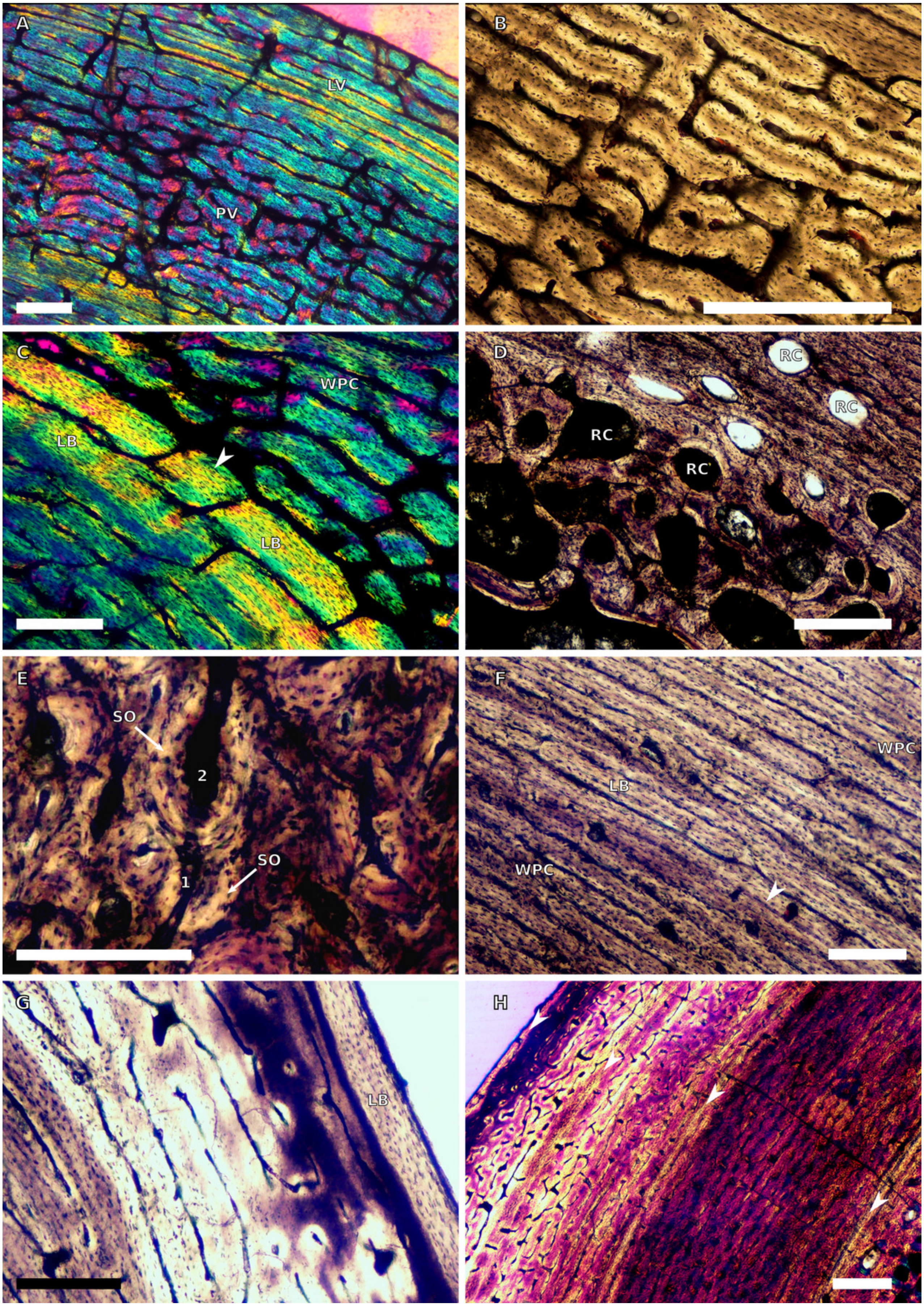
A
LV
PV
B
C
WPC
LB
LB
D
RC
RC
RC
RC
E
SO
2
SO
1
F
WPC
LB
WPC
G
LB
H

Figure 9

Figure 9: SC2 and SC3 tibial osteohistology.

A, overview in normal light of the cortex of BP/1/4751C (SC2) showing resorption cavities distributed from the inner to the outer cortex, scale bar = 500 µm. B, high magnification in normal light of the mid- and outer cortex of BP/1/4751C (SC2) showing a WPC with annuli of parallel-fibred bone associated with LAGs, scale bar = 500 µm. C, high magnification in cross-polarised light of the mid-cortex of BP/1/5108B (SC3) showing a WPC, scale bar= 200 µm. D, high magnification in normal light of the mid-cortex of BP/1/4928B (SC3) showing secondary osteons up to two generations, scale bar = 250 µm. E, high magnification in cross-polarised light of the mid- and outer cortex of BP/1/4928B (SC3) showing a high level of remodelling in the mid-cortex and a possible EFS in the outer cortex, scale bar = 1000 µm. F, high magnification in cross-polarised light of the outer cortex of BP/1/4928B (SC3) showing LAGs resembling an EFS of parallel-fibred bone, scale bar= 500 µm. G, high magnification in normal light of the outer cortex of BP/1/5108B (SC3) showing a slight decrease in vascularization, scale bar = 500 µm. H, overview in normal light of the outer cortex of BP/1/5108B (SC3) showing LAG distribution, scale bar = 1000 µm. White arrowheads indicate single LAGs. Abbreviations: MC, medullary cavity; PFB, parallel-fibred bone; PO, primary osteon; RC, resorption cavity; SO, secondary osteon; WPC, woven-parallel complex.

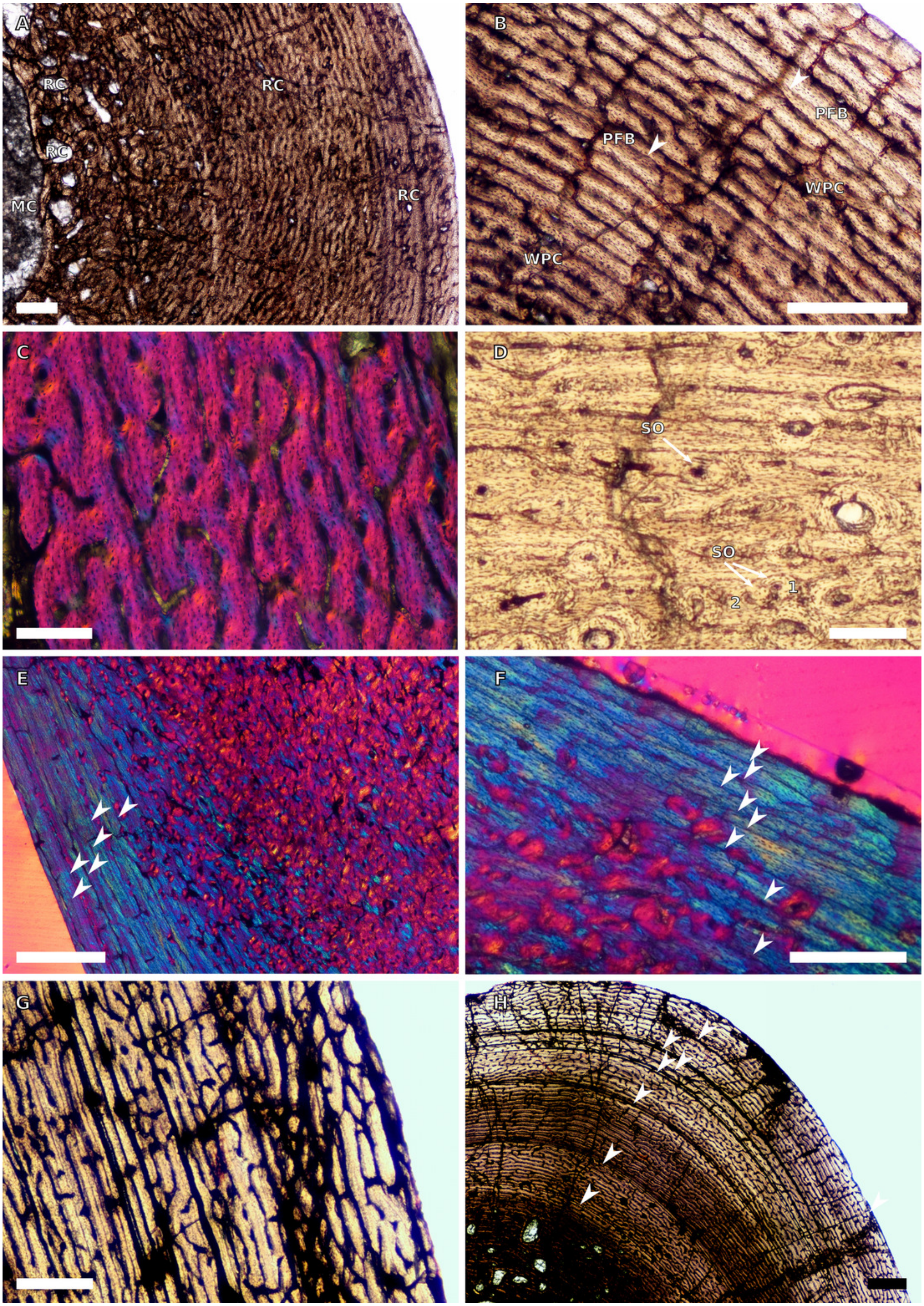
A
RC
RC
RC
RC
MC
B
PFB
PFB
WPC
WPC
C
D
SO
SO
1
2
E
F
G
H

Figure 10

Figure 10: SC3 Fibula osteohistology.

A, high magnification in cross-polarised light of the inner cortex of BP/1/4928 showing secondary osteons and resorption cavities, scale bar = 500 µm. B, high magnification in cross-polarised light of the mid-cortex of BP/1/4928 showing multiple generations of secondary osteons, scale bar = 300 µm. C, high magnification in normal light of the mid-cortex of BP/1/4928C showing a laminar vascular arrangement and a WPC with two LAGs, scale bar = 250 µm. D, high magnification in normal light of the outer cortex of BP/1/4928 showing an EFS, scale bar = 250 µm. E, overview in normal light of BP/1/4928C showing LAG distribution and EFS in bracket, scale bar= 1000 µm. F, high magnification in normal light of the inner to mid-cortex of BP/1/4998 showing longitudinal canals with short anastomoses, scale bar= 500 µm. G, high magnification in normal light of the outer cortex of BP/1/4998 showing a decrease in vascularization, scale bar = 500 µm. H, overview in normal light of the cortex of BP/1/4998 showing LAG distribution, scale bar = 1000 µm. White arrowheads indicate single LAGs; yellow arrowheads indicate double LAGs. Abbreviations: MC, medullary cavity; PO, primary osteon; RC, resorption cavity; SO, secondary osteon; WPC, woven-parallel complex.

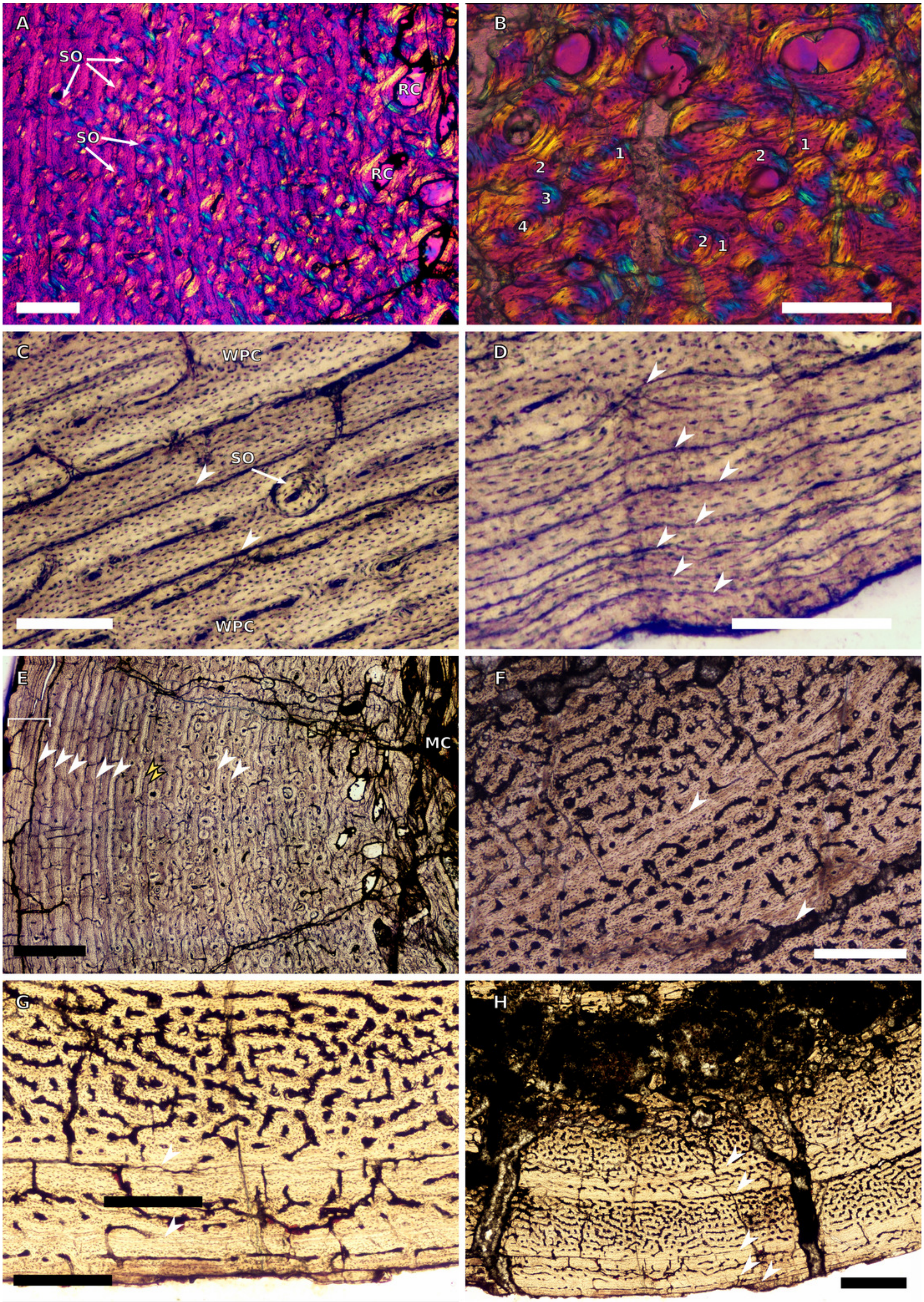
A
SO
SO
RC
RC
B
1
2
1
2
3
4
2
1
C
WPC
SO
WPC
D
E
MC
F
G
H

Figure 11

Figure 11: Spacing between the medullary cavity margin, CGMs and the sub-periosteal surface, expressed as a percentage of total cortex thickness.

A, SC1 specimens. B, SC2 specimens. C, SC3 specimens. D, SC4 specimens. The first, pink bar represents the proportional distance from the medullary cavity (0 on the y-axis) to the first LAG, which can be affected by resorption and remodelling. The last red bar represents the proportional distance between the last recorded LAG and the sub-periosteal margin, which records the last and possibly incomplete interval of growth for the specimen. Other bar colours represent the inter-LAG distances between the first and *n*th LAG. Specimens are arranged left to right from smallest to largest.

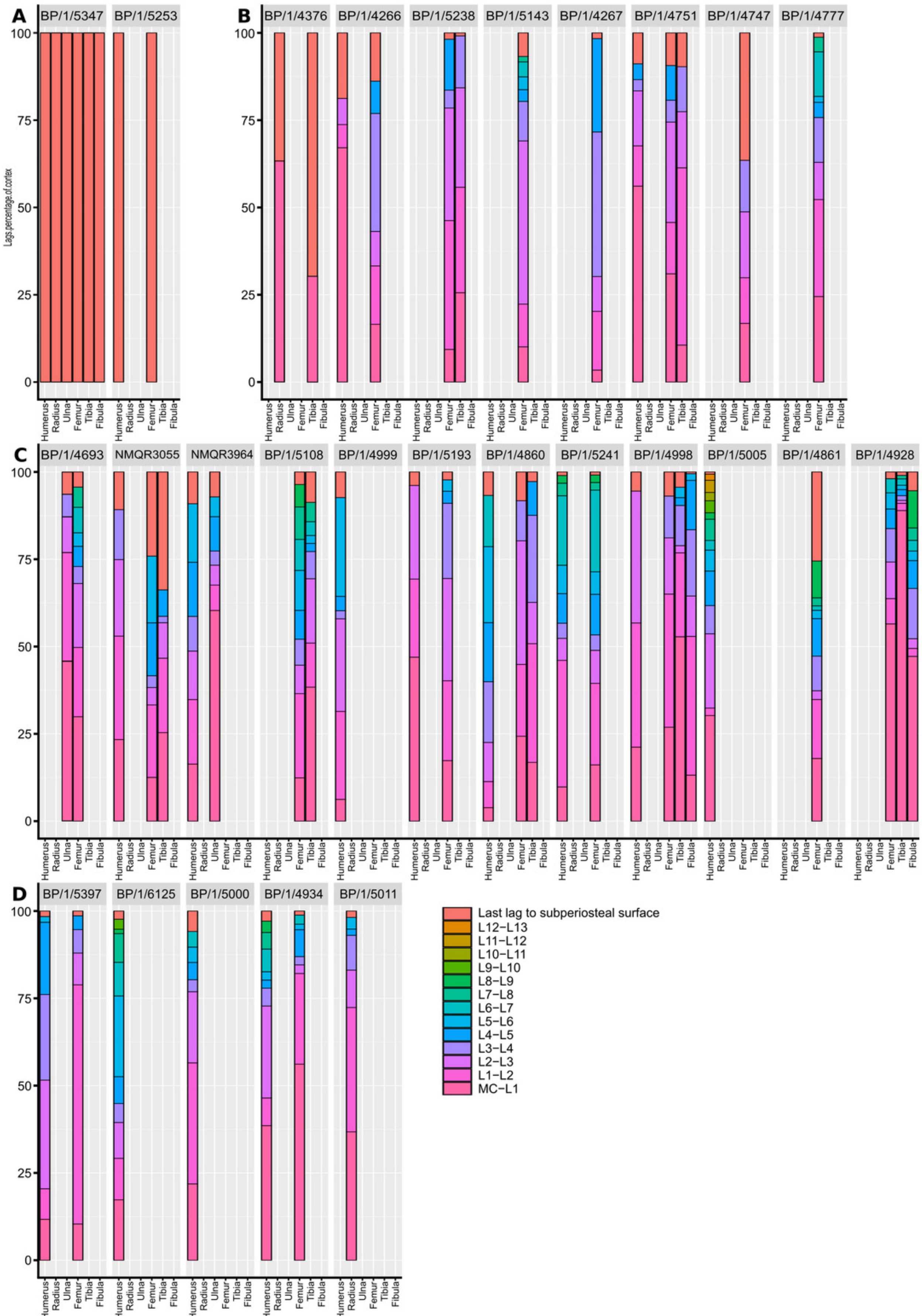
A
B
C
D
BP/1/5347
BP/1/5253
BP/1/4376
BP/1/4266
BP/1/5238
BP/1/5143
BP/1/4267
BP/1/4751
BP/1/4747
BP/1/4777
BP/1/4693
NMQR3055
NMQR3964
BP/1/5108
BP/1/4999
BP/1/5193
BP/1/4860
BP/1/5241
BP/1/4998
BP/1/5005
BP/1/4861
BP/1/4928
BP/1/5397
BP/1/6125
BP/1/5000
BP/1/4934
BP/1/5011
Lags.percentage.of.cortex
100
75
50
25
0
Humerus
Radius
Ulna
Femur
Tibia
Fibula
Last lag to subperiosteal surface
L12−L13
L11−L12
L10−L11
L9−L10
L8−L9
L7−L8
L6−L7
L5−L6
L4−L5
L3−L4
L2−L3
L1−L2
MC−L1

Figure 12

Figure 12: Relationship between circumference, cortical thickness, number of CGMs and proportional vascularisation.

A, Relationship between Log(cortical thickness) and Log(circumference) in the femur. B, Relationship between Log(cortical thickness) and Log(circumference) in the humerus. C, Relationship between Log(cortical thickness) and Log(circumference) in the tibia. D, Relationship between number of LAGs and circumference in the femur. E, Relationship between number of LAGs and circumference in the humerus. F, Relationship between number of LAGs and circumference in the tibia. G, Relationship between proportional vascularisation and circumference in the femur. H, Relationship between proportional vascularisation and circumference in the humerus. I, Relationship between proportional vascularisation and circumference in the tibia. J, Relationship between number of humeral LAGs and number of femoral LAGs. K, Relationship between proportional humeral vascularisation and proportional femoral vascularisation.

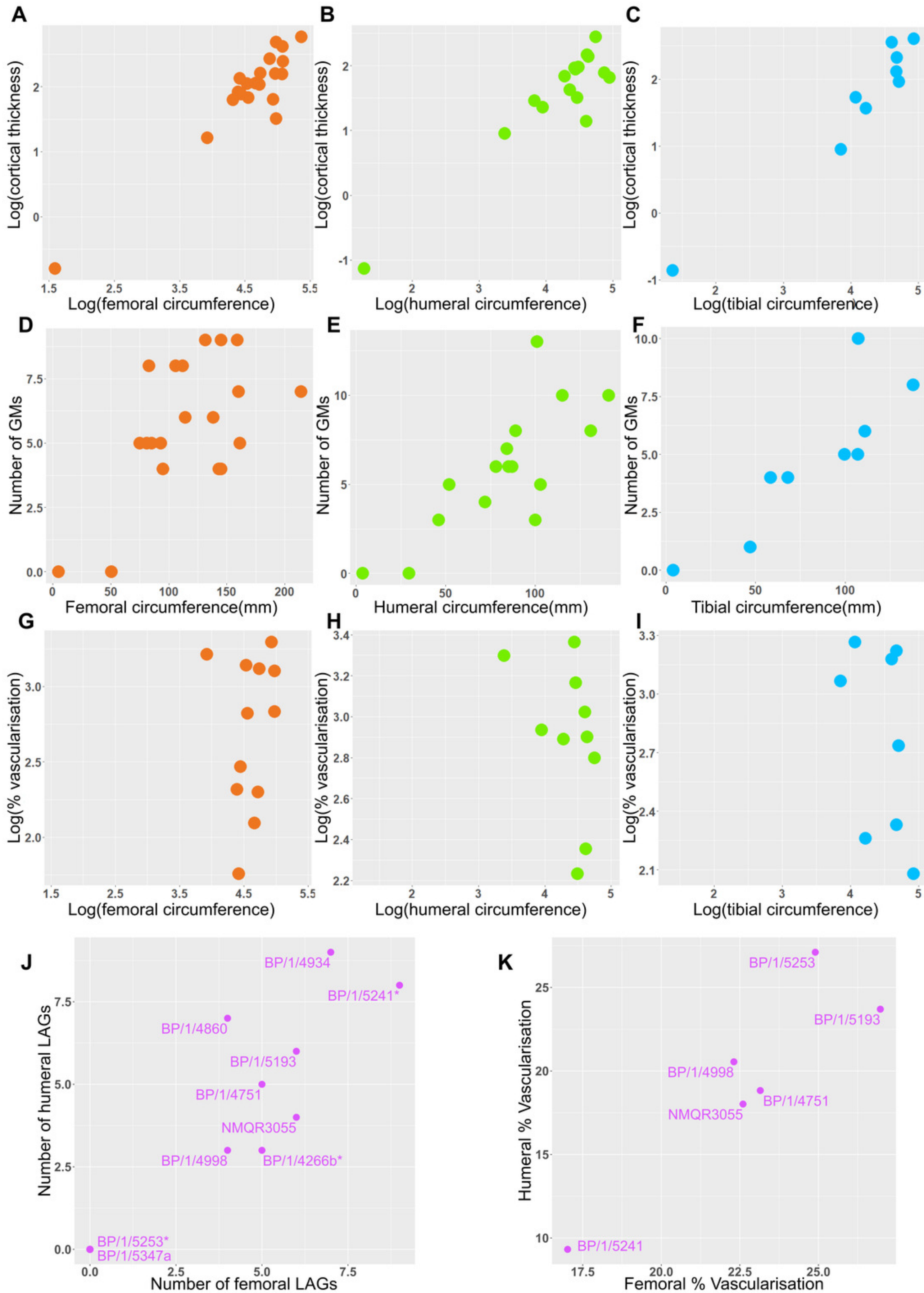
A
B
C
Log(cortical thickness)
Log(femoral circumference)
Log(humeral circumference)
Log(tibial circumference)
D
E
F
Number of GMs
Femoral circumference(mm)
Humeral circumference(mm)
Tibial circumference(mm)
G
H
I
Log(% vascularisation)
J
K
Number of humeral LAGs
Number of femoral LAGs
BP/1/4934
BP/1/5241*
BP/1/4860
BP/1/5193
BP/1/4751
NMQR3055
BP/1/4998
BP/1/4266b*
BP/1/5253*
BP/1/5347a
Humeral % Vascularisation
Femoral % Vascularisation
BP/1/5253
BP/1/5193
BP/1/4998
BP/1/4751
NMQR3055
BP/1/5241

Figure 13

Figure 13: Approximated growth curves of *Massospondylus carinatus* using femoral LAG radii as a proxy for body size.

A, Actual measurements of a growth series of femora (circles) and humeri (triangles). B, Estimated minimum age growth curve based on femora. C, Estimated maximum age growth curve based on humeri. D, LAG radius vs LAG number in all femora. E, LAG radius vs LAG number in all tibiae.

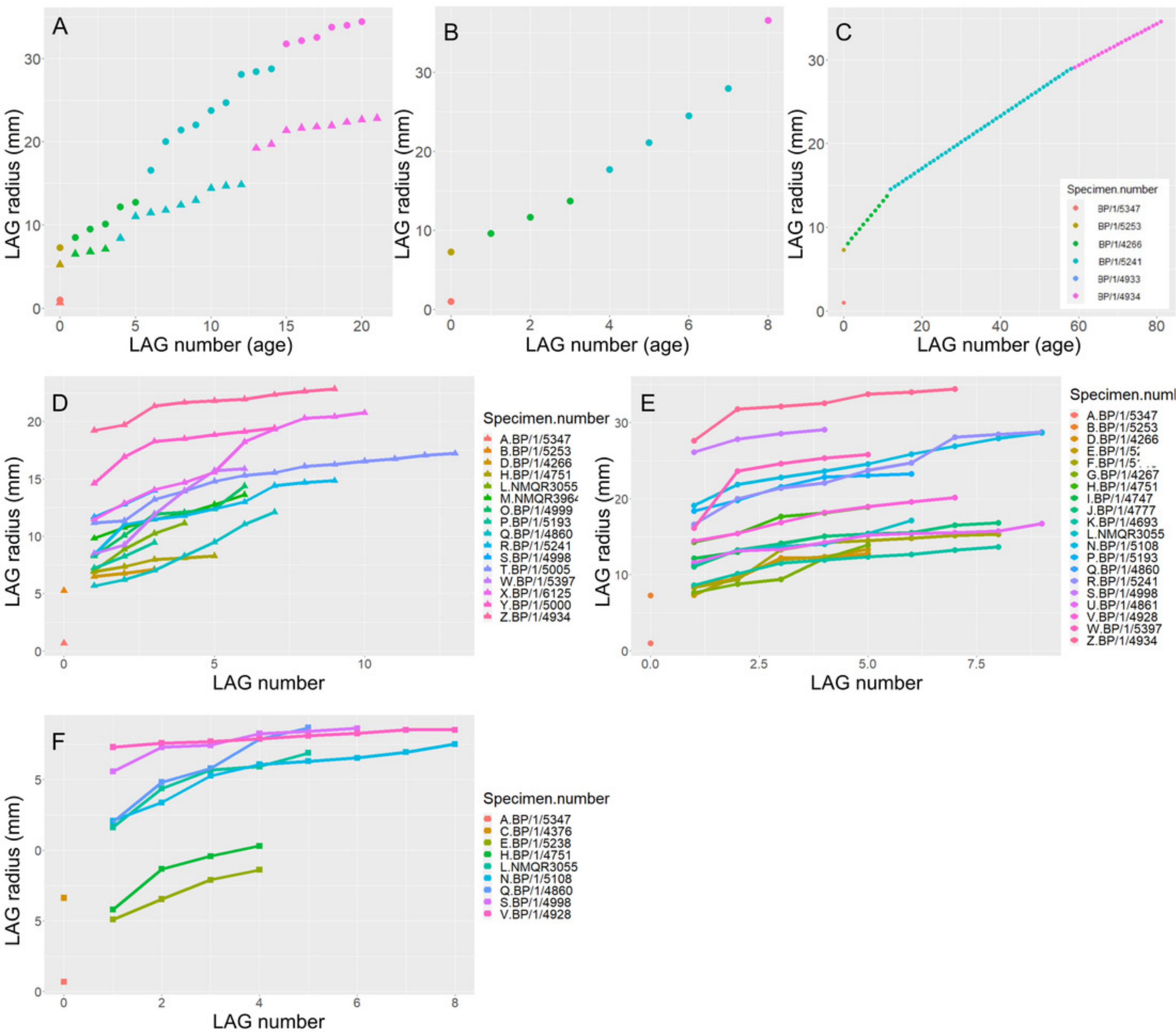
A
B
C
LAG radius (mm)
LAG number (age)
Specimen.number
BP/1/5347
BP/1/5253
BP/1/4266
BP/1/5241
BP/1/4933
BP/1/4934
D
E
F
LAG number
A.BP/1/5347
B.BP/1/5253
D.BP/1/4266
H.BP/1/4751
L.NMQR3055
O.BP/1/4999
P.BP/1/5193
Q.BP/1/4860
R.BP/1/5241
S.BP/1/4998
T.BP/1/5005
W.BP/1/5397
X.BP/1/6125
Y.BP/1/5000
Z.BP/1/4934
E.BP/1/5238
G.BP/1/4267
I.BP/1/4747
J.BP/1/4777
K.BP/1/4693
N.BP/1/5108
U.BP/1/4861
V.BP/1/4928
C.BP/1/4376